Available online at www.sciencedirect.com
ScienceDirect
International Journal of Mass Spectrometry 255–256 (2006) 279–300
International Journal of Mass Spectrometry
www.elsevier.com/locate/ijms

The most reactive third-row transition metal: Guided ion beam and theoretical studies of the activation of methane by Ir^+

Feng-Xia Li, Xiao-Guang Zhang, P.B. Armentrout *

Chemistry Department, University of Utah, 315 S. 1400 E. Rm 2020, Salt Lake City, UT 84112, United States

Received 7 January 2006; received in revised form 22 February 2006; accepted 23 February 2006
Available online 29 March 2006

Abstract

The potential energy surface for activation of methane by the third-row transition metal cation, Ir^+, is studied experimentally by examining the kinetic energy dependence of reactions of Ir^+ with methane, $IrCH_2^+$ with H_2 and D_2, and collision-induced dissociation of $IrCH_2^+$ with Xe using guided ion beam tandem mass spectrometry. A flow tube ion source produces Ir^+ in its electronic ground state term and primarily in the ground spin–orbit level. We find that dehydrogenation to form $IrCH_2^+ + H_2$ is exothermic, efficient, and the only process observed at low energies for reaction of Ir^+ with methane, whereas IrH^+ dominates the product spectrum at higher energies. We also observe the IrH_2^+ product, which provides evidence that methane activation proceeds via a dihydride $(H)_2IrCH_2^+$ intermediate. The kinetic energy dependences of the cross sections for several endothermic reactions are analyzed to give 0 K bond dissociation energies (in eV) of $D_0(Ir^+–2H) > 5.09 \pm 0.07$, $D_0(Ir^+–C) = 6.59 \pm 0.05$, $D_0(Ir^+–CH) = 6.91 \pm 0.23$, and $D_0(Ir^+–CH_3) = 3.25 \pm 0.18$. $D_0(Ir^+–CH_2) = 4.92 \pm 0.03$ eV is determined by measuring the forward and reverse reaction rates for $Ir^+ + CH_4 \rightleftharpoons IrCH_2^+ + H_2$ at thermal energy. Ab initio calculations at the B3LYP/HW+/6-311++G(3df,3p) level performed here show reasonable agreement with the experimental bond energies and with the few previous experimental and theoretical values available. Theory also provides the electronic structures of the product species as well as intermediates and transition states along the reactive potential energy surfaces. We also compare this third-row transition metal system with the first-row and second-row congeners, Co^+ and Rh^+. Differences in reactivity and mechanisms can be explained by the lanthanide contraction and relativistic effects that alter the relative size of the valence s and d orbitals.

Keywords: Bond energy; C–H bond activation; Guided ion beam; Iridium; Methane

1. Introduction

Iridium complexes are good homogeneous C–H bond activation catalysts in solution [1], and react by an oxidative addition mechanism at an unsaturated Ir center. This special reactivity of Ir is reflected in the gas phase where, using a Fourier-transform ion cyclotron resonance (FTICR) spectrometer, Irikura and Beauchamp found that Ir^+ dehydrogenates CH_4 with 70% efficiency, the highest among all the transition metal cations [2]. In order to develop more efficient and economical homogeneous catalysts, we need to understand the various factors that contribute to such specialized reactivity. For this purpose, gas-phase studies are a good starting point for providing information on the intrinsic properties of metals in the absence of solvent and stabilizing ligands. Such studies also form an ideal interface for theoretical calculations on such complicated elements, providing benchmark information to guide theory of more complex systems.

Considerable research has been done to study the reactions of the first-row and second-row transition metal ions (M^+) with hydrogen and small hydrocarbons in the gas phase, i.e., in the absence of solvent, stabilizing ligands, and metal supports [3,4]. Among the experimental techniques available for measuring thermodynamics of gas-phase species, the guided ion beam methods used in our laboratory can examine reactions at hyperthermal energies, and thereby have the ability to study endothermic reactions. This permits the determination of the bond dissociation energies (BDEs) for $M^+–C_xH_y$ ($x = 0$–3, $y = 0$–$2x + 2$) [4]. The thermochemistry obtained from these studies is of obvious fundamental interest and is relevant to a variety of catalytic reactions involving transition metal systems [5,6]. Such ion beam studies also provide insight into the electronic requirements for the activation of methane by transition metal ions and periodic trends in this reactivity. We have applied

* Corresponding author. Tel.: +1 801 581 7885; fax: +1 801 581 8433.
E-mail address: armentrout@chem.utah.edu (P.B. Armentrout).

1387-3806/$ – see front matter © 2006 Elsevier B.V. All rights reserved.
doi:10.1016/j.ijms.2006.02.021

this methodology to all the first-row and second-row transition metals except Tc [3,7–18] and more recently to several of the third-row metals as well [18–21]. A significant advantage of these comprehensive studies is the comparison of bond energies and reactivities of all transition-metal complexes, thereby establishing periodic trends. A particularly interesting feature of the third-row transition metals is the study of the influence of strong spin–orbit coupling on the reactivity.

In this study, we report results for the reactions of Ir^+ with CH_4 and CD_4, $IrCH_2^+$ with H_2 and D_2, and collision-induced dissociation (CID) of $IrCH_2^+$ with Xe over a wide range of kinetic energies. These reactions allow us to examine both exothermic and endothermic processes, probe the potential energy surface, and provide mechanistic information complementary to previous experimental and theoretical work. Theoretical calculations are also performed to assign electronic structures and explore potential energy surfaces and possible mechanisms. These are compared to previous results [2,22–24], in particular, the theoretical studies of Perry et al. [25] and those of Musaev and Morokuma [26], who examined the complete potential energy surface for the $[Ir, C, 4H]^+$ system.

2. Experimental and theoretical

2.1. Instrumentation

The guided ion beam tandem mass spectrometer on which these experiments were performed has been described in detail previously [27]. Briefly, reactant ions are generated in a direct current discharge flow tube source described below [28]. The ions are extracted from the source, accelerated, and focused into a magnetic sector momentum analyzer for mass selection of the primary reactant ions. Mass-selected ions are decelerated to a desired kinetic energy and focused into an octopole ion beam guide, which uses radio-frequency electric fields to trap the ions in the radial direction and ensure complete collection of reactant and product ions [29,30]. The octopole passes through a static gas cell that contains the reaction partner at a low pressure (usually $\leq$0.3 mTorr) so that multiple ion–molecule collisions are improbable. All products reported here result from single bimolecular encounters, as verified by pressure dependence studies. Product and unreacted primary ions drift to the end of the octopole where they are extracted, focused, passed through a quadrupole mass filter for mass analysis, and subsequently detected with a secondary electron scintillation ion detector using standard pulse counting techniques. Ion intensities are converted to absolute cross sections after correcting for background signals [31]. Absolute uncertainties in cross section magnitudes are estimated to be $\pm$20%.

The kinetic energy dependence of the ions is varied in the laboratory frame by scanning the dc bias on the octopole with respect to the potential of the ion source region. Ion kinetic energies in the laboratory frame, E_{lab}, are converted to energies in the center-of-mass frame, E_{CM}, using the formula $E_{CM} = E_{lab}m/(m+M)$, where m and M are the neutral and ionic reactant masses, respectively. All energies reported below are in the CM frame unless otherwise noted. Two effects broaden the cross section data: the thermal motion of the neutral reactant gas (Doppler broadening) and the kinetic energy distribution of the reactant ion [32,33]. The absolute zero and distribution of the ion kinetic energies are determined using the octopole beam guide as a retarding potential analyzer as described previously [31]. The distribution of ion kinetic energies is nearly Gaussian and has a typical FWHM between 1.0 and 1.4 eV (lab) in these studies. The uncertainties in the absolute energy scale are $\pm$0.05 eV (lab).

2.2. Ion source

Atomic iridium metal cations are formed in a direct current discharge flow tube (DC/FT) source [28]. This source consists of a cathode held at high negative voltage (0.7–1.5 kV) over which a flow of approximately 90% He and 10% Ar passes at a total pressure of 0.3–0.5 Torr and ambient temperature. The cathode in this work is iridium foil attached to an iron holder. Ar^+ ions created in the discharge are accelerated toward the metal cathode, thereby sputtering Ir^+ ions. These ions are then swept down a 1 m long flow tube. The flow conditions used in this ion source provide about 10^5 thermalizing collisions between an ion and He ($\sim 10^4$ collisions with Ar) before the ions enter the guided ion beam apparatus. Generally, these conditions have been found to thermalize the ions, thereby producing atomic ions in their ground electronic state. For example, on the basis of comparisons to a surface ionization source, the DC/FT source was found to generate Sc^+ [34], Fe^+ [35], Co^+ [36], Ni^+ [37], Ru^+ [38], Rh^+ [38], and Pd^+ [38] ions with an average electronic temperature of 700 ± 400 K, and Y^+, Zr^+, Nb^+, and Mo^+ ions with an average electronic temperature of 300 ± 100 K [39]. The populations of Ir^+ ions created under such conditions have been discussed in a previous paper [57], and rely on energies taken from spectroscopic work of Van Kleef and Metsch [40]. Most Ir^+ ions are in the ground electronic state, a^5F_5 ($6s^15d^7$), even at the highest likely temperature. From the populations of ions at 700 ± 400 K, the average electronic energy is calculated to be only $0.002 + 0.013/-0.002$ eV for Ir^+.

$IrCH_2^+$ is produced by the introduction of CH_4 into the flow tube about 15 cm downstream of the discharge zone at a pressure of $\sim$2 mTorr. Three-body collisions with the He/Ar flow gas stabilize and thermalize the ions both rotationally and vibrationally. These ions are presumed to be in the ground electronic state and the internal energy of these complexes should be well described by a Maxwell–Boltzman distribution of rotational and vibrational states corresponding to 300 ± 100 K. Previous studies from this laboratory have shown that these assumptions are usually valid for molecular species [4].

2.3. Data analysis

The kinetic-energy dependence of product cross sections is analyzed to determine E_0, the energy threshold for product formation at 0 K. E_0 differs from the apparent threshold observed under laboratory conditions because of the kinetic and internal energy distributions of the reactants. These contributions allow reactions to occur at energies below E_0. To determine E_0,

Table 1
Parameters of Eq. (1) used in modeling the reaction cross-sections

Reactants	Products	σ_0	n	E_0 (eV)	$D_0(Ir^+–L)$ (eV)
$Ir^+ + CD_4$	$IrD^+ + CD_3$	4.67 ± 0.53	1.64 ± 0.24	1.69 ± 0.07	2.87 ± 0.07
	$IrD_2^+ + CD_2$	0.22 ± 0.09	1.34 ± 0.16	4.20 ± 0.04	0.62 ± 0.04
	$IrC^+ + 2D_2$	0.97 ± 0.01	1.09 ± 0.09	1.60 ± 0.03	6.60 ± 0.03
	$IrCD^+ + D_2 + D$	0.35 ± 0.13	1.20 ± 0.01	2.36 ± 0.14	6.89 ± 0.14
	$IrCD_3^+ + D$	0.11 ± 0.02	1.38 ± 0.29	1.53 ± 0.11	3.05 ± 0.11
$Ir^+ + CH_4$	$IrH^+ + CH_3$	5.19 ± 0.78	1.67 ± 0.11	1.61 ± 0.06	2.87 ± 0.06
	$IrH_2^+ + CH_2$	0.48 ± 0.04	1.50 ± 0.22	4.05 ± 0.09	0.66 ± 0.09
	$IrC^+ + 2H_2$	0.83 ± 0.05	1.09 ± 0.09	1.48 ± 0.05	6.58 ± 0.05
	$IrCH^+ + H_2 + H$	0.37 ± 0.02	1.07 ± 0.28	2.09 ± 0.20	6.98 ± 0.20
	$IrCH_3^+ + H$	0.14 ± 0.02	1.10 ± 0.14	1.50 ± 0.07	2.98 ± 0.07
$IrCH_2^+ + Xe$	$Ir^+ + CH_2$	0.16 ± 0.03	1.64 ± 0.21	6.71 ± 0.20	6.71 ± 0.20
$IrCH_2^+ + D_2$	$IrCHD_2^+ + H$	0.02 ± 0.01	1.82 ± 0.02	1.45 ± 0.10	3.18 ± 0.10[a]
	$IrC^+ + H_2 + D_2$	4.14 ± 0.13	0.88 ± 0.02	2.42 ± 0.15	5.86 ± 0.15
$IrCH_2^+ + H_2$	$IrCH_3^+ + H$	0.13 ± 0.04	1.53 ± 0.11	1.71 ± 0.12	2.98 ± 0.12[a]
	$IrC^+ + 2H_2$	2.61 ± 0.05	1.00 ± 0.00	2.32 ± 0.06	5.96 ± 0.15

[a] Bond energy for Ir^+–CHD_2 or Ir^+–CH_3.

endothermic reaction cross sections are modeled using Eq. (1) [4,41–43],

$$\sigma(E) = \sigma_0 \sum g_i(E + E_i + E_{el} - E_0)^n / E, \quad (1)$$

where σ_0 is an energy-independent scaling factor, E the relative kinetic energy of the reactants, and n is an adjustable parameter. There is an explicit sum of contributions from rovibrational states of reactants at 300 K, denoted by i, having energies E_i and populations g_i, where $\sum g_i = 1$. The various sets of vibrational frequencies and rotational constants used to determine E_i in this work are taken from the literature for H_2 [44], D_2 [44], CH_4 [45], and CD_4 [45] and from our ab initio calculations for $IrCH_2^+$. As noted above, E_{el} at 700 ± 400 K is believed to be 0.002 + 0.013/−0.002 eV for Ir^+ and thus is negligible. Before comparison with the experimental data, Eq. (1) is convoluted with the kinetic energy distributions of the ions and neutral reactants at 300 K [31]. The σ_0, n, and E_0 parameters are then optimized using a nonlinear least-squares analysis to give the best reproduction of the data [31]. Error limits for E_0 are calculated from the range of threshold values for different data sets over a range of acceptable n values combined with the absolute uncertainty in the kinetic energy scale and electronic energy.

2.4. Theoretical calculations

In general, quantum chemistry calculations reported here are computed using the B3LYP hybrid density functional method [46,47] and performed with the GAUSSIAN 98 and 03 suites of programs [48,49]. The B3LYP functional was used for all the calculations done here because it provides reasonable results for the analogous Pt^+, W^+, and Re^+ with CH_4 systems [19–21]. In all cases, the thermochemistry reported here is corrected for zero-point energy effects using unscaled frequencies. Because several of the transition states of interest here involve bridging hydrogens, the rather large 6-311++G(3df,3p) basis set is used for carbon and hydrogen. This basis set gives good results for the thermochemistry of methane and dihydrogen, with deviations from experiment of less than 0.08 eV for the bond energy of H–CH_3 (4.406 eV versus 4.478 eV), H_2–CH_2 (4.666 eV versus 4.713 eV), H–CH (4.332 eV versus 4.360 eV), C–H (3.532 eV versus 3.465 eV), and H–H (4.505 eV versus 4.478 eV). (See Table 1 of [19] for experimental thermochemistry used for all H, D, CH_x, and CD_x species.) The 60 core electrons of iridium are described by the relativistic effective core potential (ECP) of Hay-Wadt (HW) [50], with the valence electrons described by the Los Alamos double zeta (LANL2DZ) basis set. This basis set is optimized for neutral atoms, whereas the positive charge differentially contracts the s orbitals compared to the d orbitals. Hence, calculations were performed with an altered HW-ECP basis set for Ir^+ as described by Ohanessian et al. (HW+) [51]. Explicit spin–orbit calculations are beyond the scope of the present study and are not included here.

The most appropriate choice for a level of theory has been thoroughly investigated for the first and third row transition metal methyl cations by Holthausen et al. [23] and for first-row transition row metal methylene cations by Holthausen et al. [52]. In the first study, these authors used B3LYP, Beck-Half-and-Half-LYP (BHLYP), and QCISD(T) methods with a basis set consisting of a polarized double-zeta basis on C and H and the Hay-Wadt relativistic ECP with valence electrons added. The symmetries of the metal methyl species were constrained to C_{3v}. For the first row MCH_3^+ species (M = Sc–Cu), where experimental results are available for all metals [4], these authors conclude that the B3LYP functional overbinds, with a mean absolute deviation (MAD) from experiment of 0.41 eV. The BHLYP functional and the QCISD(T) methods perform more accurately, with MADs of 0.18 and 0.20 eV, respectively. For the third row elements, the bond energies calculated using B3LYP were again higher than those for BHLYP and QCISD(T). In contrast, for the metal methylene complexes [52], the BHLYP functional predicts bond energies consistently below experimental values, whereas the performance of the B3LYP functional is quite good. In addition, these authors found that the results depended on the basis

set used for the metal ion with an all electron basis providing better results than effective core potential (ECP) methods. On the basis of these results, the present study includes calculations for the various product ions using the B3LYP and BHLYP functionals with both the HW+ and Stuttgart/Dresden (SD) ECP [53] for Ir^+, along with QCISD(T)/HW+ calculations. Such calculations will be explicitly noted, but unless otherwise designated, our results will refer to a B3LYP/HW+/6-311++G(3df,3p) level of theory.

Using the HW+ basis set and the B3LYP level of theory, we calculate a ^5F ground state for Ir^+, with a ^3F state at 0.30 eV. The excitation to the lowest lying triplet state was found to be 0.36 eV at the BHLYP/HW+ level of theory and 0.20 eV for QCISD(T)/HW+. These calculated triplet excitation energies can be favorably compared to the experimental value of 0.40 eV [40], where the experimental splitting is taken from the statistical mean of the various spin–orbit states for ^5F and ^3F. For the present studies, it is also important to locate the singlet state, however, the experimental singlet state energy is not particularly well defined because the strong spin–orbit interactions mix the singlet states with the lower-lying high spin states. For example, the lowest experimental energy level having primarily singlet character (65%) lies at 4.06 eV, but even the first excited state at 0.28 eV (primarily $^3F_4$) has 4% singlet character and the second excited state (primarily $^3P_2$) at 0.38 eV has 17% singlet character. Likewise the B3LYP theoretical calculations find two singlet states (both $5d^8$ configurations and assigned to ^{1}D/G), one showing substantial spin contamination, $s(s+1) = 1.60$, at 0.65 eV and another with no spin contamination at 1.95 eV. When using the SD basis set, a triplet ground state is found for Ir^+ at both the B3LYP and BHLYP levels of theory, with the quintet state higher by 0.14 and 0.19 eV, respectively. The singlet state lies at 1.68 and 1.83 eV, respectively. However, QCISD(T)/SD calculations again give a quintet ground state for Ir^+, with a triplet state at 0.42 eV, and a singlet state at 1.18 eV.

Experimental BDEs refer to the ground spin–orbit state at 0.0 eV, a^5F_5 for Ir^+ [40]. In contrast, calculations are referenced to the statistically weighted mean of all spin–orbit levels in the ground state term, 0.642 eV for Ir^+ (a^5F) [40]. Because our calculations do not explicitly include spin–orbit interactions, it is possible that calculated bond energies should be corrected by this different asymptotic energy before comparison with experimental values. Because spin–orbit effects influence the energetics of all reactants, intermediates, and products, we do not apply corrections in the present work as the magnitude of the effects are unknown for the products. This implicitly assumes that the spin–orbit corrections largely cancel. This assumption has been tested for the $W^+ + CH_4$ system where Maitre and coworkers had explicitly calculated spin–orbit interactions ranging from 0.06 to 0.29 eV for several tungsten-containing molecular ions compared to the 0.51 eV value for atomic W^+ [54]. These results indicate that spin–orbit effects are likely to reduce the theoretical bond energies in the present work but by less than the 0.64 eV value associated with the atomic ion. Likewise Balasubramanian and Dai [55] find that spin–orbit coupling stabilizes the ground state of IrH_2^+ by 0.38 eV, such that the spin–orbit correction for this species would only be 0.26 (=0.64–0.38) eV.

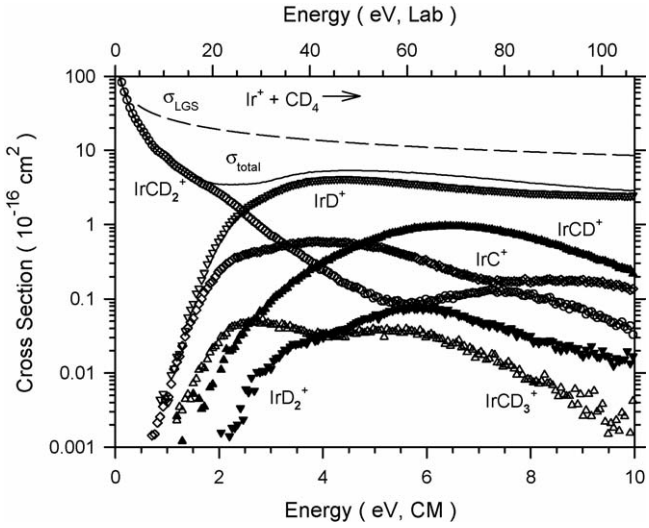

Fig. 1. Cross sections for reaction of Ir^+ ($^5F_5$) with CD_4 as a function of kinetic energy in the center-of-mass frame (lower axis) and laboratory frame (upper axis). The full line shows the total cross section and the dashed line shows the LGS collision cross section.

3. Experimental results

3.1. Reactions of Ir^+ with methane

Fig. 1 shows cross sections for the reaction of Ir^+ with CD_4, which yields product ions as shown in reactions (2)–(7).

$$Ir^+ + CD_4 \rightarrow IrD^+ + CD_3 \quad (2)$$

$$\rightarrow IrD_2{}^+ + CD_2 \quad (3)$$

$$\rightarrow IrCD_3{}^+ + D \quad (4)$$

$$\rightarrow IrCD_2{}^+ + D_2 \quad (5)$$

$$\rightarrow IrCD^+ + D + D_2 \quad (6)$$

$$\rightarrow IrC^+ + 2D_2 \quad (7)$$

Studies of the reaction of Ir^+ with CH_4 were also performed and yielded results consistent with those shown in Fig. 1. Only results from the perdeuterated species are presented here because CD_4 reduces mass overlap and allows intensities of the various product ions to be measured more accurately over a great energy range.

As can be seen from Fig. 1, dehydrogenation to form $IrCH_2^+ + H_2$ is the only process observed at low energies, consistent with previous ICR studies [2] at thermal energies. The cross section for dehydrogenation of CD_4 to produce $IrCD_2^+$ decreases with increasing energy, indicating an exothermic reaction having no barrier in excess of the energy of the reactants. This reaction cross section declines approximately as $E^{-0.5\pm0.1}$ below 0.2 eV, comparable to the prediction of the Langevin–Gioumousis–Stevenson (LGS) collision cross section [56] which has an $E^{-0.5}$ energy dependence. The magnitudes of the experimental and LGS collision cross sections are the same within the ±20% uncertainty in the absolute magnitudes. In order to compare the reaction efficiency measured

here with previous results, our cross section is converted to a rate constant by the following expression, $k(\langle E\rangle) = v\sigma(E)$, where $v = (2E/\mu)^{1/2}$ and $\mu = mM/(m+M)$, the reduced mass of the reactants. The rate constants depend on the mean energy of the reactants, which includes the average thermal motion of the neutral, such that $\langle E\rangle = E + (3/2)\gamma k_B T$, where $\gamma = M/(m+M)$. As discussed in a previous paper [31], the rate $k(\langle E\rangle)$ has the property that it approaches the thermal rate constant for the effective temperature $T' = \gamma T$, which equals 277 K for the present results, as $v \to 0$. Because the guided ion beam technique allows very low ion energies, the kinetic and internal energy distributions of the reactants are dominated by the thermal distributions of the neutral reactant such that a true thermal rate constant at this temperature can be obtained directly from the cross section data at the lowest energy. Using this equation, we obtain $k = 9.7 \pm 2.0 \times 10^{-10}$ cm^3/s for reaction with CH_4 and $k = 9.8 \pm 2.0 \times 10^{-10}$ cm^3/s for reaction with CD_4. These values are higher than literature rate constants obtained by ICR mass spectrometry of $7.0 \pm 1.8 \times 10^{-10}$ cm^3/s for CH_4, and $7.0 \pm 1.8 \times 10^{-10}$ cm^3/s for CD_4 [2] but within the experimental errors. Compared to the LGS collision rate, we find the reactions with CH_4 and CD_4 occur with efficiencies of $99 \pm 20\%$ and $111 \pm 23\%$, respectively, again within experimental error of the ICR results, $71 \pm 18\%$ and $80 \pm 20\%$, respectively [2].

Between energies of 0.2 and 1.5 eV, the $IrCD_2^+$ cross sections decline as $E^{-1.3\pm0.1}$. At still higher energies (>1.5 eV), the $IrCD_2^+$ cross section begins to decline more rapidly. There are four possible decomposition pathways to account for this decline, which include decomposition into $IrC^+ + D_2$, $IrCD^+ + D$, $IrD^+ + CD$, and $Ir^+ + CD_2$. The magnitudes of the cross sections for IrC^+ and $IrCD^+$ account for some of this decline, but not quantitatively. Decomposition of $IrCD_2^+$ to $Ir^+ + CD_2$ and $IrD^+ + CD$ cannot begin until 4.82 and 6.09 eV, respectively [19], too high to account for the decline. We therefore infer that the decrease in the $IrCD_2^+$ cross section must be attributed to competition with formation of IrD^+, which is most easily explained if these two products share a common intermediate, as discussed below.

Formation of IrD^+ and $IrCD_3^+$ arise from similar apparent thresholds near 1 eV, which indicates that the Ir^+–D and Ir^+–CD_3 single bonds have similar bond energies. However, formation of IrD^+ dominates the product spectrum at high energies because of angular momentum effects [9–11,18], as discussed below, and also because $IrCD_3^+$ dissociates to $IrCD^+ + D_2$. This dehydrogenation requires 1.02 ± 0.29 eV according to the thermochemistry determined below. At higher energies, $IrCD_3^+$ can also dissociate to $IrCD_2^+ + D$, which accounts for the second feature in the $IrCD_2^+$ cross-section beginning near 5.5 eV.

IrC^+ product ions have the lowest energy threshold among all the endothermic products observed, indicating that they are formed by elimination of molecular deuterium from $IrCD_2^+$. Other possible pathways for IrC^+ formation that stem from either $IrCD_3^+$ or $IrCD^+$ require much higher energies than the dehydrogenation of $IrCD_2^+$. The second feature in this cross section beginning near 7.0 eV arises from the second feature in the $IrCD_2^+$ cross-section, i.e., the neutral products are $D_2 + 2D$.

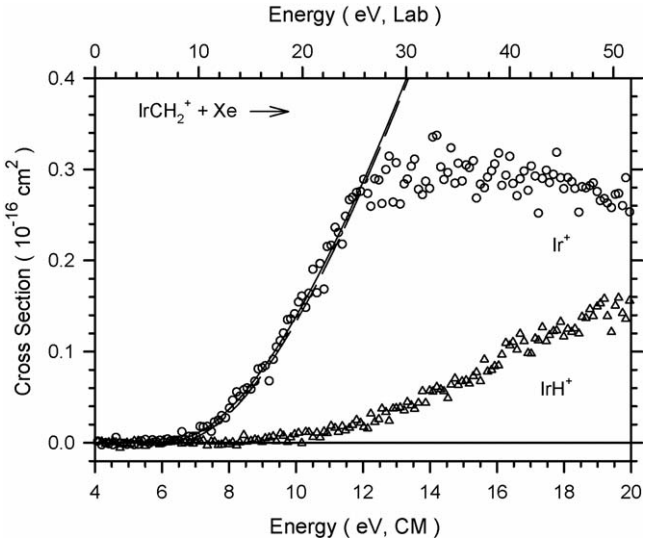

Fig. 2. Cross sections for collision-induced dissociation of $IrCH_2^+$ with Xe as a function of kinetic energy in the center-of-mass frame (lower axis) and laboratory frame (upper axis). The best fit to the data using Eq. (1) incorporating RRKM modeling for the reactants with an internal temperature of 0 K is shown as a dashed line. The solid line shows this model convoluted over the kinetic and internal energy distributions of the reactant neutral and ion.

Formation of IrD_2^+ has the highest threshold of all processes observed, which is consistent with formation of the high-energy CD_2 neutral. The formation of MD_2^+ product ions is unusual and has not been detected for reaction of methane with first-row [8–10,12–15,18], second-row [7,11,16–18], and several third-row (La^+, W^+, Re^+, Lu^+) transition metal ions [18,20,21]. However, this product has been observed in reactions of methane with Pt^+ [19].

3.2. $IrCH_2^+ + Xe$

The exothermic dehydrogenation reaction analogous to reaction 5 provides only a lower limit to the BDE of $IrCH_2^+$ of 4.71 eV = $D_0(H_2\text{–}CH_2)$. To measure an upper limit to this BDE, we performed a collision-induced dissociation (CID) experiment. Fig. 2 shows cross sections for the interaction of Xe with $IrCH_2^+$. Reactions (8) and (9) were the only processes observed.

$$IrCH_2^+ + Xe \rightarrow Ir^+ + CH_2 + Xe \quad (8)$$

$$\rightarrow IrH^+ + CH + Xe \quad (9)$$

The dominant process is the simple CID process that cleaves the Ir^+–CH_2 bond and has an apparent threshold between 6 and 7 eV. At higher energies, a small amount of reaction (9) is also observed. As noted above, the lowest energy decomposition process of $IrCH_2^+$ is dehydrogenation, requiring 1.67 ± 0.06 eV according to the thermochemistry determined below. Unfortunately, under the conditions needed for efficient ion transmission, the mass resolution in our quadrupole mass filter is particularly poor on the low mass side of all peaks. Therefore, because of the proximity of the very intense $IrCH_2^+$ reactant ion, measurement of $IrCH^+$ and IrC^+ intensities was very difficult and no reliable cross sections could be obtained.

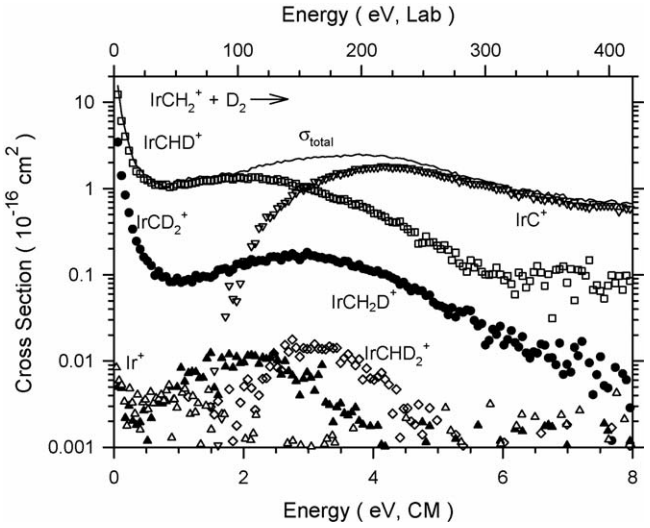

Fig. 3. Cross sections for the bimolecular reaction of $IrCH_2^+$ with D_2 as a function of kinetic energy in the center-of-mass frame (lower axis) and laboratory frame (upper axis). The full line shows the total product cross section. As discussed in the text, one product channel (closed circles) can be attributed to the $IrCD_2^+$ product at low energies and partially to $IrCH_2D^+$ at higher energies. The cross sections for the $IrCH_2^+ + H_2$ (D_2) → $Ir^+ + CH_4$ (CH_2D_2) reactions are shown by open (closed) triangles.

3.3. $IrCH_2^+ + D_2$

Fig. 3 shows cross sections for reaction of $IrCH_2^+$ with D_2, which yields six product ions, as shown in reactions (10)–(13).

$$IrCH_2^+ + D_2 \rightarrow IrCH_2D^+ + D \quad (10a)$$

$$\rightarrow IrCHD_2^+ + H \quad (10b)$$

$$\rightarrow IrCD_2^+ + H_2 \quad (11a)$$

$$\rightarrow IrCHD^+ + HD \quad (11b)$$

$$\rightarrow IrC^+ + H_2 + D_2 \quad (12)$$

$$\rightarrow Ir^+ + CH_2D_2 \quad (13)$$

The reaction of $IrCH_2^+$ with H_2 was also studied, yielding $IrCH_3^+$, IrC^+, and Ir^+ product ions. Results for $IrCH_2^+ + D_2$ are shown here because use of D_2 permits the hydrogen scrambling reactions to be observed, although Fig. 3 shows the cross sections for formation of Ir^+, process (13), in both the H_2 (open triangles) and D_2 (closed triangles) systems.

Because the $IrCH_2D^+$ and $IrCD_2^+$ products have the same mass, their cross sections cannot be independently measured. However, their cross sections should have similar kinetic energy dependences to those of $IrCHD_2^+$ and $IrCHD^+$, respectively. Further, the magnitude of the cross section of $IrCH_3^+$ from reaction of $IrCH_2^+$ with H_2 has approximately the same magnitude (0.12 Å^2) at about 3 eV compared to that of $IrCH_2D^+$ (0.18 Å^2) in the reaction of $IrCH_2^+ + D_2$. Therefore, the exothermic part of this cross section below 1 eV is unambiguously attributed to $IrCD_2^+$, whereas contributions from both ions are anticipated above about 1.5 eV.

Reactions (11a) and (11b) are exothermic because of zero-point energy differences, specifically by 0.072 and 0.038 eV, respectively. We find that these reaction cross sections decline approximately as $E^{-1.4}$ and $E^{-1.0}$, respectively, below 0.8 eV. The rate constants for these two reactions at thermal energy (0.04 eV) are $k = 1.6 \pm 0.3 \times 10^{-10}$ cm^3/s and $k = 3.8 \pm 0.8 \times 10^{-10}$ cm^3/s, respectively, compared to a collision (LGS) rate constant of 10.6×10^{-10} cm^3/s. Thus, the overall efficiency of the observed reactions is 51 ± 10%, which means that the return to reactants accounts for the other 50% of the reactivity. If dehydrogenation of a transiently formed $IrCH_2D_2^+$ intermediate were statistically controlled, then the expected ratio of $IrCH_2^+$:$IrCHD^+$:$IrCD_2^+$ products would be 1:4:1, whereas the observed ratio is approximately 3:2:1 at thermal energies. As the collision energy is increased, the ratio increases in favor of reforming $IrCH_2^+$ and $IrCD_2^+$ formation declines compared to $IrCHD^+$ formation.

We find that reaction (13) and its perprotio analogue exhibit no apparent energy barriers. The magnitude of this cross section is only about 0.005 ± 0.001 Å^2 near thermal energies (0.008 ± 0.002 Å^2 for reaction with H_2), falling to about 0.002 (0.004) Å^2 by 0.4 eV. This converts to a thermal rate constant for reaction (13) of $k = 0.9 \pm 0.2 \times 10^{-13}$ cm^3/s ($1.5 \pm 0.3 \times 10^{-13}$ cm^3/s for reaction with H_2), which is only 0.009 ± 0.002 (0.010 ± 0.002)% of the LGS collision rate. At energies above 0.5 eV, the cross sections for Ir^+ product formation in the reactions of $IrCH_2^+$ with H_2 and D_2 differ, Fig. 3. In the reaction with H_2, the Ir^+ cross section decreases monotonically as the energy increases, whereas the D_2 system exhibits a cross section that rises near 0.5 eV and reaches a peak around 2.0 eV. Similar behavior was observed in the reactions of $PtCH_2^+$ with H_2 and D_2, where again formation of Pt^+ in the D_2 reaction exhibits both exothermic and endothermic features, while in the H_2 system, the Pt^+ cross section declines monotonically [19]. In contrast, production of W^+ in the reactions of WCH_2^+ with H_2 and D_2 exhibits only exothermic cross sections [21]. Because of the complexity of the isotope exchange process, discussed further below, the origins of the endothermic feature are unclear.

We also observe the IrC^+ product with an apparent threshold of about 1.5 eV. This appears to be formed by decomposition of the $IrCHD^+$ (primarily) and $IrCD_2^+$ products. $IrCD^+$ might also be formed in this reaction; however, it cannot be detected because it has the same mass as the $IrCH_2^+$ reactant. Likewise $IrCH^+$ might be formed, but its proximity to the intense $IrCH_2^+$ reactant makes this product difficult to detect as well.

4. Thermochemical and theoretical results

The endothermic cross sections for each product ion are analyzed using Eq. (1), as described above, and the optimum values of the parameters are listed in Table 1. Because this model explicitly includes rotational, translational, and vibrational energy distributions, all E_0 thresholds determined by Eq. (1) correspond to 0 K values. From the measured thresholds, the BDEs of the iridium–ligand cations can be calculated using Eq. (14),

$$D_0(Ir^+\text{–L}) = D_0(\text{R–L}) - E_0 \quad (14)$$

Table 2
Comparison of experimental and theoretical 0 K thermochemistry for IrH^+ and $IrCH_x^+$ ($x = 0$–4) species

Species	This work						Previous work	
	Exp	Theory[a]					Exp	Theory
		B3LYP		BHLYP		QCISD(T)		
		HW+	SD	HW+	SD	HW+		
Ir^+–H ($^4\Sigma^-$)	3.12 ± 0.06[b]	3.25	3.30	2.92	3.00	3.05		2.85,[c] 3.10 [d], 2.71, 3.14 [e]
Ir^+–CH_3 ($^4A_2$)	3.25 ± 0.18	3.26	3.47	2.75	3.02	3.19		3.01[d], 3.13 ± 0.22[f], (3.10 ± 0.22)[f]
Ir^+–CH_2 ($^3A_2$)	4.92 ± 0.03	5.21	4.83	4.36	3.95	5.03	>4.71[g]	5.33 ± 0.22[h], 5.16 ± 0.13[i], 4.90[j]
Ir^+–CH ($^2\Delta$)	6.91 ± 0.23	6.50	6.68	5.15	5.46	6.67		7.11[h]
Ir^+–C ($^1\Sigma^+$)	6.59 ± 0.05	6.38	6.88	4.97	5.56	6.58		
Ir^+–H_2 ($^3A_2$)	>0.61 ± 0.07	1.89	2.12	1.32	1.63	1.67		>0.95,[g] 1.72[d], 0.74 (1.30)[k]

[a] Calculations use the 6-311++G(3df,3p) basis set on C and H and the indicated ECP on Ir^+. HW+ = Hay-Wadt [50] as adjusted for the cation by Ohanessian et al. [51]. SD = Stuttgart-Dresden [53].
[b] [57].
[c] [51].
[d] [58].
[e] [59].
[f] [23] BHLYP (QCISD(T)).
[g] [2].
[h] [22].
[i] [25].
[j] [26].
[k] [55] CASSCF (MRSDCI).

where the D_0(R–L) values can be calculated using the heats of formation summarized previously [19]. This equation assumes that there are no activation barriers in excess of the endothermicity of a given reaction, an assumption that is often true for ion–molecule reactions because of the long-range attractive forces [31,43]. Table 2 provides a summary of the BDEs derived and a comparison with literature values, as discussed below. Tables 3 and 4 provide summaries of the B3LYP theoretical results (energies and structures) for each of the product ions and their excited states. These results are discussed in detail in the following sections for each species.

4.1. Ir^+–H

We have recently measured the bond energy of 3.12 ± 0.06 for IrH^+ from the reactions of Ir^+ with H_2 and D_2 [57]. From Eq. (14), D_0(D–CD_3) = 4.58 eV, and a calculated zero-point energy difference between IrD^+ and IrH^+ of 0.041 ± 0.004 eV, this predicts a threshold of 1.42 ± 0.06 eV for formation of IrD^+ in reaction (2). Our analysis of this cross section (Table 1) measures a somewhat higher threshold of 1.69 ± 0.07 eV. Similarly, the predicted E_0 value for the IrH^+ product ion obtained in the methane system is 1.36 ± 0.06 eV, whereas the measured threshold is 1.61 ± 0.06 eV. Thus, the CH_4 and CD_4 systems behave similarly to each other but do not agree with the thermodynamic results obtained from the H_2 and D_2 systems. On average, the thresholds in the methane systems are higher in energy by 0.26 ± 0.13 eV, a discrepancy that can be attributed to a competitive shift. Reaction (5) strongly competes with reaction (2) at its threshold, whereas there are no competing channels in the reactions of Ir^+ with H_2 and D_2. This competition can delay the apparent onset for formation of IrD^+ (IrH^+) in the methane systems. Indeed, simplified phase space calculations of the coupled reactions confirm that such a competitive shift occurs in the methane reactions with a magnitude comparable to that deduced here. Because this reaction system involves several intermediates and coupling between surfaces of different spin (see below), a quantitative reproduction of these data using phase space theory is not feasible.

GVB calculations indicate that IrH^+ has a $^4\Sigma^-$ ground state with a covalent bond formed between a sd hybridized (37% 6s and 63% 5d) orbital on Ir^+ (a ^{5}F) and the 1s orbital on H [51]. These calculations find a 0 K BDE for IrH^+ of 2.85 eV [51], which Perry later updated to 3.10 eV [58]. Dai et al. (DHB) [59] also calculated a $^4\Sigma^-$ ground state with D_e(Ir^+–H) of 2.85 eV (FOCI) and 3.28 eV (MRSDCI). After correcting for the zero-point energy of 0.14 eV for IrH^+ (from our calculation for the $^4\Sigma^-$ ground state), this gives 0 K BDEs of 2.71 eV (FOCI) and 3.14 eV (MRSDCI).

Overall, these values are in reasonable agreement with our experimental value of 3.12 ± 0.06 eV [57]. Our calculations find a BDE of 3.25 (3.30) eV when using the B3LYP functional, 2.92 (3.00) eV for BHLYP, and 3.05 eV for QCISD(T) using the HW+ (SD) basis sets on Ir [57]. As found by Holthausen et al. for the third-row transition metal ion methyl cations [23], the B3LYP functional overbinds compared to the BHLYP and QCISD(T) methods. The bond lengths determined here are 1.570 Å (B3LYP) and 1.565 Å (BHLYP), which are in excellent agreement with values from Ohanessian et al. [51], 1.560 Å, and from DHB [59], 1.567 Å (FOCI) and 1.548 Å (MRSDCI).

GVB [51] calculations indicate that there is a low-lying $^4\Phi$ state lying only 0.16 eV above the $^4\Sigma^-$ ground state. They suggest that spin–orbit coupling could alter the order of these states such that the $^4\Phi$ state probably becomes the ground state. DHB [59] calculated that the $^4\Phi$ state lies only 0.19 eV (FOCI) and 0.20 eV (MRSDCI) above the $^4\Sigma^-$ ground state. In our cal-

Table 3
Theoretical energies of reactants and products calculated at the B3LYP/HW+/6-311++G(3df,3p) level of theory

Compound	State	$s(s+1)$[a]	Energy (E_h)	Zero-point energy (E_h)	E_{rel} (eV)[b]
H	^2S	0.75	−0.502257		
H_2	$^1\Sigma_g^+$	0.00	−1.180030	0.010064	
C	^3P	2.00	−37.857442		
CH	$^2\Pi$	0.75	−38.495898	0.006450	0.000
	$^4\Sigma^-$	3.75	−38.462172	0.006943	0.931
CH_2	$^3B_1$	2.01	−39.167949	0.017169	
CH_3	$^2A''$	0.75	−39.857664	0.029685	
CH_4	$^1A_1$	0.00	−40.536527	0.044525	
Ir^+	^5F	6.00	−104.254004		0.000
	^3F	2.39	−104.2429757		0.300
	$^1D/G$	1.60*	−104.2301746		0.648
	$^1D/G$	0.00	−104.1825016		1.946
IrH^+	$^4\Sigma^-$	3.76	−104.881018	0.005177	0.0
IrH_2^+	$^3A_2$	2.01	−105.505763	0.012457	0.0
IrC^+	$^1\Sigma^+$	0.00	−142.348722	0.002670	0.0
	$^3\Delta$	2.01	−142.344009	0.002403	0.121
	$^3\Sigma^-$	2.03	−142.285954	0.002133	1.693
	$^3\Pi/^3\Phi$	2.15	−142.251381	0.001991	2.630
	$^3\Pi$	3.03*	−142.225236	0.001600	3.331
$IrCH^+$	$^2\Delta$	0.77	−142.993581	0.013175	0.0
	$^2\Sigma^+$	0.75	−142.9913906	0.013158	0.059
	$^4A''$	3.76	−142.949147	0.010536	1.137
	$^4A'$	3.76	−142.948603	0.010534	1.152
	$^2\Pi/^2\Phi$	1.78*	−142.9348001	0.011050 (−689)	1.542
	$^2\Pi/^2\Phi$	1.70*	−142.9304309	0.011109 (−698)	1.662
$IrCH_2^+$	$^3A_2$	2.03	−143.619524	0.02316	0.0
	$^3A_1$	2.03	−143.617865	0.023153	0.045
	$^3B_2$	2.05	−143.598592	0.022545	0.553
	$^3B_1$	2.05	−143.597735	0.021981	0.561
	$^1A_1$	0.00	−143.589334	0.022644	0.807
	$^5A'$	6.01	−143.555111	0.020066	1.669
	$^5A_1$	6.01	−143.554619	0.018960 (−394)	1.652
	$^5A''$	6.01	−143.554055	0.021141	1.727
	$^5B_1$	6.04	−143.501844	0.021883	3.167
	$^5A_2$	6.04	−143.384022	0.022223	6.383
	$^5B_2$	6.39	−143.290935	0.019156 (−267)	8.832
$IrCH_3^+$	$^4A_2$	3.76	−144.236071	0.034137	0.0
	$^2A''$	1.69*	−144.217796	0.033901	0.491
	$^2A'$	1.65*	−144.209742	0.034366	0.723

[a] Values indicating spin contamination are marked by an asterisk.
[b] Energy relative to the ground state species for each molecule including zero-point energies (unscaled).

culations, the $^4\Phi$ state is 0.27 (B3LYP), 0.20 (BHLYP), and 0.28 eV (QCISD(T)//BHLYP) above the $^4\Sigma^-$ ground state using the HW+ basis sets on Ir. We also determined excitation energies for a number of other excited states, as described in detail elsewhere [57].

4.2. Ir^+–CH_3

The BDE of Ir^+–CD_3 determined from the CD_4 system is 3.05 ± 0.11 eV and the BDE of Ir^+–CH_3 from the CH_4 system is 2.98 ± 0.07 eV. After correcting for the zero-point energy differences in these two values (0.027 eV), we obtain a weighted average of 2.99 ± 0.12 eV for the BDE of Ir^+–CH_3. Because this value is similar to the BDE Ir^+–H obtained from a routine analysis of the IrH^+ and IrD^+ channels, this confirms that a single bond to Ir^+ is formed in each molecule. As noted above, because there is competition with the dehydrogenation reaction, the BDE of IrH^+ determined from methane systems is too small and a similar result seems likely for $IrCH_3^+$. However, we can use the shift determined for IrH^+ (0.26 ± 0.13 eV) to give our best estimate of the $IrCH_3^+$ bond energy as 3.25 ± 0.18 eV. This is equivalent to measuring that the thresholds for $IrCH_3^+$

Table 4
Theoretical structures of reactants and products calculated at the B3LYP/HW+/6-311++G(3df,3p) level of theory[a]

Compound	State	r(Ir–H)	r(Ir–C)	r(C–H)	∠HIrH	∠IrCH	∠HCH	∠Dihedral
H_2	$^1\Sigma_g^+$							
CH	$^2\Pi$			1.122				
	$^4\Sigma^-$			1.093				
CH_2	$^3B_1$			1.078			135.1	
CH_3	$^2A''$			1.078(3)			120.0(3)	
CH_4	$^1A_1$			1.088(4)			109.5(6)	
IrH^+	$^4\Sigma^-$	1.570						
IrH_2^+	$^3A_2$	1.555			71.3			
IrC^+	$^1\Sigma^+$	1.630						
	$^3\Delta$	1.680						
	$^3\Sigma^-$	1.755						
	$^3\Pi/^3\Phi$	1.734						
	$^3\Pi$	1.845						
$IrCH^+$	$^2\Delta$		1.675	1.094		180.0		
	$^2\Sigma^+$		1.660	1.092		180.0		
	$^4A''$		1.776	1.099		136.9		
	$^4A'$		1.776	1.100		136.6		
	$^2\Pi/^2\Phi$		1.786	1.085		180.0		
	$^2\Pi/^2\Phi$		1.768	1.085		180.0		
$IrCH_2^+$	$^3A_2$		1.836	1.092(2)		121.6(2)	116.9	180.0
	$^3A_1$		1.837	1.093(2)		121.6(2)	116.9	180.0
	$^3B_2$		1.840	1.093(2)		121.6(2)	116.8	180.0
	$^3B_1$		1.837	1.093(2)		121.6(2)	116.7	180.0
	$^1A_1$		1.806	1.095(2)		120.8(2)	118.4	180.0
	$^5A'$		1.937	1.092(2)		115.7(2)	121.3	149.0
	$^5A_1$		1.931	1.088(2)		117.6(2)	124.9	180.0
	$^5A''$		1.942	1.092(2)		114.8(2)	120.5	143.9
	$^5B_1$		2.059	1.096(2)		124.1(2)	111.7	180.0
	$^5A_2$		1.847	1.100(2)		121.1(2)	117.8	180.0
	$^5B_2$		1.957	1.092(2)		113.3(2)	133.4	180.0
$IrCH_3^+$	$^4A_2$		2.022	1.093(3)		106.7(3)	112.1(3)	±116.5
	$^2A''$		2.014	1.092		106.4(2)	111.3	±116.8
				1.094(2)		107.5	112.4(2)	
	$^2A'$		2.027	1.090(2)		102.0	111.0(2)	±116.3
				1.100		109.2(2)	113.7	

[a] Bond lengths are in Å. Bond angles are in degrees. Degeneracies are listed in parentheses.

($IrCD_3^+$) lie 0.13 eV below those for IrH^+ (IrD^+), indicating that the Ir^+–CH_3 bond strength exceeds that for Ir^+–H by this amount. This higher bond energy agrees nicely with a BDE for Ir^+–CHD_2 of 3.18 ± 0.10 determined in the reaction of $IrCH_2^+$ with D_2. A slightly lower value of 2.96 ± 0.12 eV is determined for Ir^+–CH_3 in the $IrCH_2^+ + H_2$ reaction. If all four values are averaged together (the first two after adjusting by the competitive shift), then an average BDE for Ir^+–CH_3 of 3.17 ± 0.15 eV is obtained, consistent with the adjusted value of 3.25 ± 0.18 eV, which we take as our most reliable determination.

Using a GVB approach, Perry calculated that $D_0(Ir^+–CH_3)$ = 3.01 eV [58]. As mentioned above, Holthausen et al. [23] carefully considered the most appropriate choice for a level of theory for the first and third-row transition metal methyl cations. B3LYP, BHLYP, and QCISD(T) levels of theory gave predicted Ir^+–CH_3 bond energies (D_e) of 3.86, 3.35, and 2.94 eV, respectively. On the basis of results for the first-row metal methyl cations compared with experimental values, empirical corrections of −0.22 and +0.16 eV were applied to the BHLYP and QCISD(T) results leading to final estimated bond energies of 3.13 and 3.10 eV with estimated errors of ±0.22 eV. These values are somewhat below our adjusted experimental value of 3.25 ± 0.18 eV, and above the uncorrected value (2.99 ± 0.12 eV), but within the uncertainties of both.

Our B3LYP and QCISD(T) calculations obtain a D_0 of 3.26 and 3.19 eV for Ir^+–CH_3, in good agreement with our adjusted experimental value. However, the BHLYP functional drops the calculated BDE to 2.75 eV (Table 2). Use of the SD ECP increases our predicted BDEs to 3.47 (B3LYP) and 3.02 (BHLYP) eV. Note that the bond energies for IrH^+ and $IrCH_3^+$ in both the experimental and theoretical results are similar (depending on the level of theory, differences of 0.0–0.17 eV), consistent with both having comparable single covalent metal–ligand bonds. Thus, whatever the origin of any discrepancy between experiment and any particular level of theory, the same discrepancy is occurring for both IrH^+ and $IrCH_3^+$,

as assumed in deriving our adjusted values for the BDE of the latter.

We find the ground state of $IrCH_3^+$ to be $^4A_2$ with C_{3v} symmetry, consistent with previous work [58]. (This state is misidentified in the Gaussian code and in [23] as $^4A_1$. The three unpaired electrons in this molecule have a $(e)^2(a_1)^1$ configuration. As discussed elsewhere [60], the properly antisymmetrized wavefunctions for an $(e)^2$ configuration lead to $^1A_1$, ^1E, and $^3A_2$ states. Upon addition of a high-spin coupled a_1 electron, the only quartet spin state is $^4A_2$, along with the doublet states, $^2A_1$, ^2E, and $^2A_2$.) The Ir–C and C–H bond lengths (2.022 and 1.093 Å) and IrCH bond angles (106.7°) calculated here (B3LYP, Table 4) differ slightly from those calculated by Perry (2.052 and 1.084 Å and 107.7°) but are comparable to those from Holthausen et al. (2.010 and 1.099 Å and 106.8°, B3LYP; 2.017 and 1.089 Å, and 107.0°, BHLYP; 2.020 and 1.095 Å and 107.7°, QCISD(T)). We also find two excited doublet states lying 0.49 and 0.72 eV above the ground state, which both have C_s symmetry, Table 3.

4.3. Ir^+–CH_2

Reaction (5) and its perprotio analogue are exothermic. This indicates that $D_0(Ir^+–CH_2) > 4.71$ eV and $D_0(Ir^+–CD_2) > 4.82$ eV, as previously concluded by Irikura and Beauchamp [2]. The threshold of 6.71 ± 0.20 eV for the dissociation of the $Ir^+–CH_2$ bond (Table 1) from the CID experiment of $IrCH_2^+$ with Xe should be viewed as an upper limit to the true BDE. Previous work in our group often finds that CID of strongly bound small molecules provide thresholds that are higher than the thermodynamic bond energies probably because of the inefficiency in the transfer of kinetic to internal energy in the collision process [61].

We confirm that the $IrCH_2^+$ BDE cannot be as strong as 6.71 ± 0.20 eV from reactions of $IrCH_2^+$ with H_2 and D_2. Formation of Ir^+ exhibits no obvious threshold in both systems (Fig. 3). Because the reaction $IrCH_2^+ + H_2 \rightarrow Ir^+ + CH_4$ is the reverse of the dehydrogenation reaction $Ir^+ + CH_4 \rightarrow IrCH_2^+ + H_2$, this observation indicates that the dehydrogenation of methane by Ir^+ must be close to thermoneutral. From the rate constants for the forward (perprotio analogue of reaction (5)) and reverse reactions at the lowest kinetic energy in our experiments, we determine an equilibrium constant K of $6500 + 3200/-2200$. From $\Delta G = -RT \ln K$, the free energy of the reaction is calculated to be -0.226 ± 0.010 eV at 298 K. The free energy can be converted to an enthalpy of reaction at 298 K of -0.18 ± 0.01 eV by using an entropic correction of 0.046 eV as determined using molecular parameters calculated here. These parameters are also used to determine the H_0–H_{298} values for reactants and products (−0.028 eV overall), leading to an enthalpy of reaction at 0 K of -0.21 ± 0.01 eV. Combining this value with $D_0(CH_2–H_2) = 4.71 \pm 0.026$ eV [19], we obtain a BDE of 4.92 ± 0.03 eV for $Ir^+–CH_2$, consistent with the lower limit of 4.71 eV.

Irikura and Goddard previously calculated that $IrCH_2^+$ has a $^3A_2$ ground state with a calculated D_e of 4.81 eV [22]. These authors also included an empirical correction of 0.52 ± 0.22 eV, leading to their final recommended 0 K bond energy of 5.33 ± 0.22 eV, which is higher than our experimental result. Excited states, $^3A_1$, $^3B_2$, $^1A_1$, $^3B_1$, and $^5A_2$, were found lying 0.07, 0.79, 0.80, 0.82, and 1.45 eV higher in energy, respectively. Using CASSCF and MRSDCI–CASSCF methods, Musaev and Morokuma (MM) [26,62] also calculated a $^3A_2$ ground state for $IrCH_2^+$ with bond energies of 3.65 eV (CASSCF) and 4.90 (MRSDCI) eV, respectively, where the latter value agrees nicely with our experimental result. Excited states, $^3A_1$, $^3B_2$, $^1A_1$, and $^3B_1$, were found to lie 0.09 (0.07), 0.82 (0.72), 0.47 (0.42), and 0.88 (0.29) eV higher in energy, respectively, using the CASSCF (MRSDCI) approaches. Perry et al. (POG) [25] calculated a D_e of 4.81 eV using the MCPF method, but their best estimated value is $D_0 = 5.16 \pm 0.13$ eV, slightly above our experimental result. Their excitation energy for the $^1A_1$ state was 0.39 eV.

The present calculations, B3LYP/HW+ (SD) and QCISD(T), also find a $^3A_2$ ground state with a bond energy of 5.21 (4.83) and 5.03 eV, respectively, in reasonable agreement with the previous theoretical values and with experiment. The BHLYP values, 4.36 (3.95) eV, are much too low. We also find four excited states, $^3A_1$, $^3B_2$, $^1A_1$, and $^3B_1$ lying 0.05, 0.55, 0.81, and 0.56 eV higher in energy, respectively. Our ground-state geometry of r(Ir–C) = 1.836 Å, r(C–H) = 1.092 Å and ∠IrCH = 121.6° (Table 4) is comparable to that calculated by Irikura and Goddard, r(Ir–C) = 1.868 Å, r(C–H) = 1.083 Å and ∠IrCH = 121.9°; Musaev and Morokuma, r(Ir–C) = 1.960 Å, r(C–H) = 1.076 Å and ∠IrCH = 120.1°; and Perry [58], r(Ir–C) = 1.838 Å and ∠IrCH = 123.8°. Our calculations also located $^5A_1$, $^5A'$, $^5A''$, $^5B_1$, $^5A_2$, and $^5B_2$ excited states lying 1.65, 1.67, 1.73, 3.17, 6.38 and 8.83 eV higher in energy than the ground state. The $^5A_1$ state is found to have an imaginary frequency (an umbrella motion) that distorts the molecule to form the $^5A'$ state. Thus, before any zero-point energy corrections, $^5A'$ is more stable than $^5A_1$, however, the zero-point energy exceeds the height of the barrier such that this state dynamically has C_{2v} symmetry.

The $^3A_2$ ground state of $IrCH_2^+$ has a valence electronic configuration of $(1a_1)^2(1b_1)^2(1b_2)^2(1a_2)^1(2a_1)^2(3a_1)^1$, where the $1a_1$ and $1b_1$ orbitals are bonding, the $1b_2$, $1a_2$ and $2a_1$ orbitals are 5d nonbonding orbitals on Ir, and the $3a_1$ orbital is a nonbonding 6s–5dσ hybrid orbital on Ir. Thus, there is a covalent double bond between Ir^+ and CH_2. The $^3A_1$, $^3B_2$, $^3B_1$, and $^1A_1$ excited states have valence electronic configurations of $(1a_1)^2(1b_1)^2(1b_2)^2(1a_2)^2(2a_1)^1(3a_1)^1$, $(1a_1)^2(1b_1)^2(1b_2)^1(1a_2)^2(2a_1)^2(3a_1)^1$, and $(1a_1)^2(1b_1)^2(1b_2)^1(1a_2)^1(2a_1)^2(3a_1)^2$, and $(1a_1)^2(1b_1)^2(1b_2)^2(1a_2)^2(2a_1)^2(3a_1)^0$, respectively. The $^5A_1$ ($^5A'$), $^5B_1$, $^5A_2$, and $^5B_2$ excited states have valence electronic configurations of $(1a_1)^2(1b_1)^2(1b_2)^1(1a_2)^1(2a_1)^2(3a_1)^1(2b_1)^1$, $(1a_1)^2(1b_1)^2(1b_2)^1(1a_2)^1(2a_1)^2(3a_1)^1(4a_1)^1$, $(1a_1)^2(1b_1)^2(1b_2)^1(1a_2)^1(2a_1)^2(3a_1)^1(2b_2)^1$ and $(1a_1)^2(1b_1)^2(1b_2)^1(1a_2)^1(2a_1)^2(2b_1)^1(2b_2)^1$, respectively, where $4a_1$ is an antibonding σ orbital, $2b_1$ is an antibonding π orbital, and $2b_2$ is a nonbonding 6p orbital. The $^5A''$ excited state has a valence electronic configuration (using the analogous C_{2v} symmetry designations) of $(1a_1)^2(1b_1)^2(1b_2)^1(1a_2)^2(2a_1)^1(3a_1)^1(2b_1)^1$, where the only difference with the $^5A_1$ state is whether the $2a_1$ ($5d_{x2-y2}$) or $1a_2$ ($5d_{xy}$) orbital is doubly occupied.

4.4. Ir^+–CH

This ion is formed by dehydrogenation of the primary $IrCH_3^+$ product. The BDE of the Ir^+–CH bond is determined to be 6.98 ± 0.20 eV from the CH_4 system and $D_0(Ir^+–CD) = 6.89 \pm 0.14$ eV from the CD_4 system. The weighted average of these two values is 6.91 ± 0.23 eV after a zero-point energy correction of 0.02 eV for the deuterated value, where the uncertainty is 2 standard deviations of the mean. We do not believe that competition with other channels is an important factor for this process because it is a subsequent step, i.e., decomposition of one of the primary ions (see below). However, the bond energy is most conservatively viewed as a lower limit to the true thermodynamic value.

Irikura and Goddard estimate a value of 7.11 eV for the Ir^+–CH bond after estimating an intrinsic bond strength and correcting for promotion and exchange energies [22], in reasonable agreement with our measured value. Our calculated value (Table 2) of 6.50 eV (B3LYP/HW+) is lower than the experimental value, whereas the B3LYP/SD and QCISD(T) values of 6.68 and 6.67 eV, respectively, are within experimental error. The values calculated using the BHLYP/HW+(SD) functional are well below experiment, 5.15 (5.46) eV (Table 2).

Our calculations find a $^2\Delta$ ground state with a geometry having r(Ir–C) = 1.675 Å and r(C–H) = 1.094 Å. Thus, a triple bond is clearly formed. The valence orbital occupation is ($1\sigma^2 1\pi^4 1\delta^3 2\sigma^2$), where the C(2s) orbital is excluded for simplicity, the 1σ orbital is a bonding combination of the $2p_z$(C) and $5d_{z2}$(Ir) orbitals, the 2σ orbital is a nonbonding 6s–$5d_{z2}$ hybrid (largely a torus surrounding the bonding axis), the 1π orbitals are the expected $2p_{x,y}$(C)–$5d_{xz,yz}$(Ir) bonding molecular orbitals, and the 1δ are pure metal $5d_{xy,x2-y2}$(Ir) orbitals. The lowest lying excited state is $^2\Sigma^+$ lying 0.06 eV higher in energy and has a ($1\sigma^2 1\pi^4 1\delta^4 2\sigma^1$) configuration. Other excited doublet states are $^2\Phi$ and $^2\Pi$ ($1\sigma^2 1\pi^4 1\delta^3 2\sigma^1 2\pi^{*1}$) lying 1.54 and 1.66 eV higher in energy, respectively. $^4A''$ and $^4A'$ excited states are also identified lying 1.14 and 1.15 eV higher than the doublet ground state. Both states have valence orbital occupations (given in terms of the equivalent $C_{\infty v}$ symmetry designations) of ($1\sigma^2 1\pi^4 1\delta^3 2\sigma^1 2\pi^{*1}$), but here, the σ–π^* excitation needed to give the high-spin forces the geometry to bend, ∠IrCH = 137° (Table 4).

4.5. Ir^+–C

Formation of IrC^+ in reaction (7) has a measured threshold of 1.60 ± 0.03 eV (Table 1) in the CD_4 system. From Eq. (14) and $D_0(CD_2–D_2) + D_0(C–D_2) = 8.20 \pm 0.01$ eV, this gives a BDE of 6.60 ± 0.03 eV for Ir^+–C. The value of E_0 for Ir^+–C obtained in the CH_4 system is 1.48 ± 0.05 eV. Using Eq. (14) and $D_0(CH_2–H_2) + D_0(C–H_2) = 8.06 \pm 0.01$ eV, this yields a BDE for Ir^+–C of 6.58 ± 0.05 eV, in good agreement with the value from the CD_4 system. Our best experimental value for $D_0(Ir^+–C)$ is the weighted average of these two values, 6.59 ± 0.05 eV, where the uncertainty is 2 standard deviations of the mean. Because formation of IrC^+ is a high-energy process in this reaction system, its threshold could be shifted to higher energies because of competition with lower energy reactions, thus the bond energy is most conservatively viewed as a lower limit to the true thermodynamic value. From reaction of $IrCH_2^+$ with D_2 and H_2 forming IrC^+, we also derive BDEs for Ir^+–C of 5.86 ± 0.15 and 5.96 ± 0.15 eV, respectively. As this is the highest energy channel in this reaction system in which the H_2 and D_2 products can carry away some energy, these values are most conservatively viewed as lower limits to the true thermodynamic value. Thus, the values obtained from CH_4 and CD_4 reaction system are our most reliable.

The experimental value obtained is in reasonable agreement with the result of the present calculations, 6.38 (B3LYP/HW+), 6.88 (B3LYP/SD), and 6.58 (QCISD(T)) eV, Table 2. The BHLYP functional yields BDEs well below experiment, 4.97 (HW+) and 5.56 (SD) eV. Clearly, the BHLYP functional provides less accurate predictions for all multiply bound species, $IrCH_2^+$, $IrCH^+$, IrC^+, compared to the B3LYP functional with MADs of about 1.31 (1.15) versus 0.29 (0.20) eV, respectively using the HW+ (SD) ECP for Ir, whereas the QCISD(T) performs better than the DFT methods with a MAD of 0.12 eV using the HW+ ECP for Ir.

Our theoretical calculations find the ground state of IrC^+ to be $^1\Sigma^+$ with an Ir–C bond length of 1.630 Å (Table 4). The $^1\Sigma^+$ ground state of IrC^+ has a valence electronic configuration of $1\sigma^2 1\pi^4 1\delta^4$, where the orbitals are comparable to those described above for $IrCH^+$. The lowest lying excited state is $^3\Delta$ lying 0.12 eV higher in energy and has a $1\sigma^2 1\pi^4 1\delta^3 2\sigma^1$ configuration. Other excited states are $^3\Sigma^-$ ($1\sigma^2 1\pi^4 1\delta^2 2\sigma^2$), $^3\Pi/^3\Phi$ ($1\sigma^2 1\pi^4 1\delta^3 2\pi^{*1}$), and $^3\Pi$ ($1\sigma^2 1\pi^4 1\delta^2 2\sigma^1 1\pi^{*1}$) lying 1.69, 2.63, and 3.33 eV higher in energy, respectively.

4.6. H–Ir^+–H

The BDE for Ir^+–D_2 in the CD_4 system is determined to be 0.62 ± 0.04 eV. Similarly, we determined a BDE of 0.66 ± 0.09 eV for Ir^+–H_2 from the CH_4 system. The calculated zero-point energy difference between these two species is 0.018 eV such that our best experimental value for $D_0(Ir^+–H_2)$ is the weighted average of these two values, 0.61 ± 0.07 eV, where the uncertainty is 2 standard deviations of the mean. However, these two reaction channels have the highest threshold of all reactions observed, and therefore compete with all other reaction channels, especially with the much more facile formation of $IrCH_2^+ + H_2$ ($IrCD_2^+ + D_2$) and $IrH^+ + CH_3$ ($IrD^+ + CD_3$). Therefore, the BDEs determined from these reactions are best viewed as lower limits.

Our B3LYP/HW+/6-311+G(3p) calculations find an inserted $^3A_2$ ground state for IrH_2^+ with a BDE of 1.89 eV relative to the Ir^+ (a^5F) + H_2 asymptote. We also determine bond energies (zero-point energy corrected) of 1.32 and 1.67 eV using the BHLYP functional and QCISD(T) method for the $^3A_2$ ground state [23]. Use of the SD basis set leads to bond energies of 2.12 (B3LYP) and 1.63 (BHLYP) eV, respectively. Using MRCI calculations, Perry [58] determined a $D_e(Ir^+–H_2)$ of 1.79 eV for the $^3A_2$ ground state. After correcting for the zero-point energies of 0.34 eV for IrH_2^+ ($^3A_2$) and 0.27 eV for H_2, this gives a 0 K BDE of 1.72 eV for the $^3A_2$ ground state, which is comparable to our

QCISD(T) and B3LYP results. Balasubramanian and Dai (BD) [55] also identified a $^3A_2$ ground state with a BDE of 0.74 and 1.30 eV relative to the Ir^+ (^5D) + H_2 asymptote at the CASSCF and MRSDCI levels of theory, respectively, in the absence of spin–orbit effects. Including spin–orbit coupling effects stabilizes this state by 0.38 eV and the ground state asymptote by ~0.3 eV, such that the adiabatic bond energy increases to about 1.4 eV (MRSDCI). As discussed in our previous paper [57], the calculations of BD and those conducted here appear to differ primarily in values for the asymptotic limit, $Ir^+ + H_2$. The geometries (bond lengths and angles) in the present calculations find that Ir–H bonds have lengths of 1.555 Å with a ∠HIrH bond angle of 71.3°, which are in excellent agreement with Perry's calculation having Ir–H bond lengths of 1.55 Å and a ∠HIrH bond angle of 71.4°, and with those of BD having Ir–H bond lengths of 1.551 (MRSDCI) and 1.573 Å (CASSCF) and a ∠HIrH bond angle of 70.2° (MRSDCI) and 69.8° (CASSCF).

4.7. Bond-energy bond-order correlation for Ir^+–CH_x bonds

One interesting way of investigating the bond order of simple metal–ligand species is to compare with organic analogues, i.e., $D_0(Ir^+–L)$ versus $D_0(L–L)$. Such a plot is shown in Fig. 4. It can be seen that the correlation is remarkably good, which indicates that Ir^+–H and Ir^+–CH_3 are single bonds, Ir^+=CH_2 is a double bond, and Ir^+≡CH is a triple bond, as confirmed by theory. (The linear regression line in Fig. 4 is constrained to include the origin to emphasize the bond-order correlation of IrL^+ versus L_2 species.) The point that lies furthest from the line is for Ir^+–C, correlated with the BDE of C_2. In this case, the Ir^+–C BDE is stronger than predicted by this simple correlation because the covalent double bond in this molecule is augmented by back-donation of an occupied 5d orbital on Ir^+ into the empty 2p orbital on C. Such an interaction cannot occur in the C_2 molecule. Also illustrated in Fig. 4 is the relatively reasonable agreement between experiment and theory: QCISD(T) for all species.

It is also interesting to compare these results to those for the first row and second row congeners, Co^+ and Rh^+. Bond energies for CoH^+, CoC^+, $CoCH^+$, $CoCH_2^+$, and $CoCH_3^+$ are 1.98 ± 0.06, 3.60 ± 0.30, 4.35 ± 0.38, 3.29 ± 0.05, and 2.10 ± 0.04 eV, respectively [4,14]. The analogous species for Rh have bond energies of 1.67 ± 0.04, 4.25 ± 0.18, 4.60 ± 0.12, 3.69 ± 0.08, and 1.47 ± 0.06 eV, respectively [11]. From this comparison, we find that the first and second row transition-metal bonded species of Co^+ and Rh^+ are much weaker than corresponding third row congeners of Ir^+. On average, the linear regression lines indicate that the bonds to Ir^+ are 56% greater than those to Co^+, and 53% greater than those to Rh^+, an effect of the lanthanide contraction.

5. Potential energy surfaces of $[Ir,C,4H]^+$

We construct the potential energy surfaces (Fig. 5) for interaction of Ir^+ with methane at the B3LYP/HW+/6-311+G(3df,3p) level of theory and include zero-point energy corrections (unscaled). In most cases, we locate transition states using relaxed potential energy surface scans along reasonable reaction pathways, followed by geometry optimization and frequency calculations to confirm the transition states. In some cases, we also use the synchronous transit-guided quasi-Newton method (QST3) [63,64]. As discussed above, the B3LYP level of theory reproduces the bond energies of Ir^+–CH_x species adequately. Thus, the relative characteristics of these surfaces are likely to be qualitatively correct, and are of the most interest here. Tables 5 and 6 provide summaries of the theoretical results (energies and structures) for each of the intermediates and transition states. Figs. 6–8 provide the structures of these intermediates and

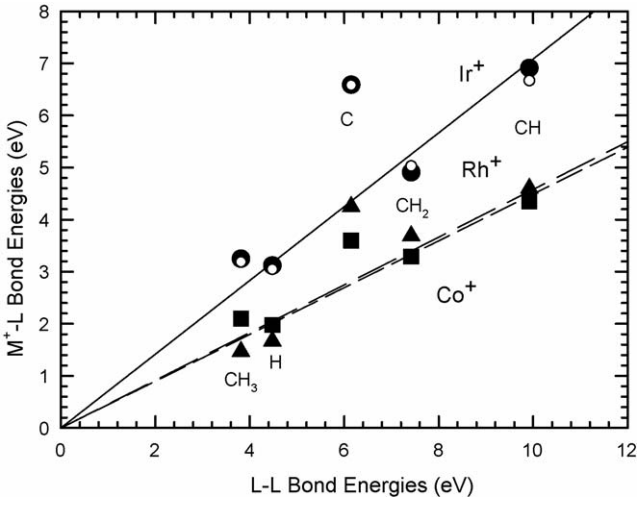

Fig. 4. Correlation of Ir^+–L bond energies with those for the organic analogues, L–L. Ir^+–L values are from Table 2 and included both experiment (closed circles) and theory (open circles, QCISD(T)). Data for Co^+ and Rh^+ (taken from Refs. [4,11,14]) are shown by squares and triangles, respectively. The lines are linear regression fits to the experiment data, excluding M^+–C, constrained to pass through the origin to emphasize the bond-order correlations.

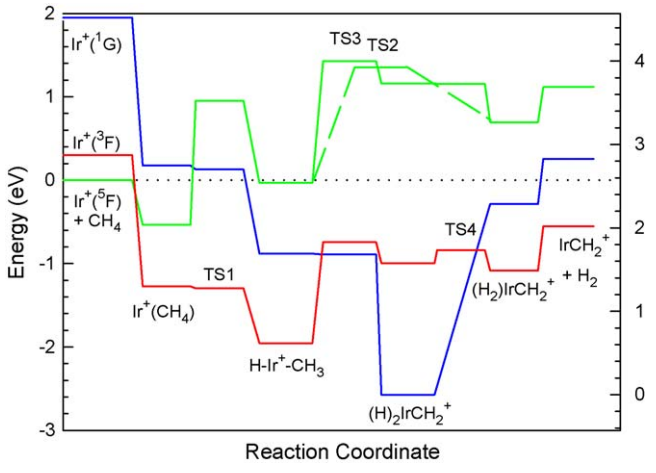

Fig. 5. $[Ir, C, 4H]^+$ potential energy surface derived from theoretical results. The relative energies of all species are based on ab initio calculations (B3LYP/HW+/6-311++G(3df,3p), see Table 5). Energies on the left are relative to the Ir^+(^5F) + CH_4 ground state asymptote, whereas those on the right are referenced to the $(H)_2IrCH_2^+$ ($^1A'$) intermediate.

Table 5
Theoretical energies of intermediates and transition states calculated at the B3LYP/HW+/6-311++G(3df,3p) level of theory

Compound	State	$s(s+1)$[a]	Energy (E_h)	Zero-point energy (E_h)[b]	E_{rel} (eV)[c]
$Ir^+ + CH_4$	$^5F + {}^1A_1$		−144.790531	0.044525	0.000
$Ir^+(CH_4)$	$^3A''$	2.00	−144.834902	0.042154	−1.272
	$^3A'$	2.00	−144.833502	0.043272	−1.203
	$^3B_2$	2.02	−144.822468	0.042322	−0.929
	$^3A_2$	2.00	−144.824055	0.044578	−0.911
	$^5A''$	6.00	−144.809333	0.043702	−0.534
	$^1A'$	0.00	−144.782291	0.042711	0.175
TS1	$^3A''$	2.00	−144.834890	0.041230 (−269)	−1.297
	^1A	0.00	−144.781849	0.040542 (−535)	0.128
	$^5A''$	6.01	−144.747141	0.036149 (−340)	0.953
$HIrCH_3^+$	$^3A''$	2.01	−144.859425	0.041603	−1.954
	$^3A''$	2.01	−144.858002	0.041532	−1.917
	$^3A'$	2.01	−144.845057	0.041935	−1.554
	$^1A'$	0.00	−144.819344	0.040975	−0.881
	$^5A''$	6.00	−144.786463	0.039221	−0.034
TS2	$^5A''$	6.01	−144.728885	0.032642 (−735)	1.354
TS3	^1A	0.00	−144.818597	0.039857 (−474)	−0.891
	^3A	2.01	−144.808640	0.035297 (−727)	−0.744
	^5A	6.01	−144.727742	0.034139 (−289)	1.426
$(H)_2IrCH_2^+$	$^1A'$	0.00	−144.880725	0.040199	−2.572
	$^3A''$	2.01	−144.819472	0.036875	−0.996
	$^5A''$	6.00	−144.738948	0.035571	1.160
TS4	^3A	2.01	−144.812230	0.035451 (−526)	−0.837
	$^5A''$	6.00	−144.737557	0.033986 (−424)	1.155
$(H_2)IrCH_2^+$	$^3A_2$	2.02	−144.824379	0.038588	−1.083
	$^1A_1$	0.95*	−144.814981	0.038609	−0.826
	$^3B_2$	2.04	−144.797710	0.035742	−0.434
	$^3B_1$	2.04	−144.796816	0.036343	−0.394
	$^1A_1$	0.00	−144.794079	0.037598 (−72)[d]	−0.285
	$^5A'$	6.00	−144.755054	0.034870	0.703
$IrCH_2^+ + H_2$	$^3A_2$	2.03	−144.799554	0.033224	−0.553
	$^1A_1$	0.00	−144.769364	0.032708	0.254
	$^5A'$	6.01	−144.735141	0.030126	1.115

[a] Values indicating spin contamination are marked by an asterisk.
[b] Imaginary frequencies (in cm^{-1}) are given in parenthesis.
[c] Energy relative to Ir^+ (^5F) + CH_4 reactants including zero-point energies (unscaled).
[d] This imaginary frequency corresponds to a C–Ir–(H_2) bend out of the plane of the molecule.

transition states on the quintet, triplet, and singlet spin surfaces, respectively.

5.1. Quintet surface

Interaction of Ir^+ (^5F, $6s^15d^7$) with methane leads initially to the formation of a $Ir^+(CH_4)$ adduct in which the methane molecule remains intact and largely unperturbed. The methane binds in an η^2 conformation in a $^5A''$ state (C_s symmetry) (Fig. 6) lying 0.53 eV below the reactant asymptote. Previous calculations identified this intermediate as a $^5B_1$ state, although C_{2v} symmetry was imposed in these studies, lying 0.39 (POG) [25] and 0.16 (MM) eV [26] below the Ir^+ (^5F) + CH_4 reactants. Upon further reduction of the Ir–H bond distance, the system passes over a transition state, ^{5}TS1, leading to the insertion intermediate H–Ir^+–CH_3. This transition state has C_s symmetry and an HIrC bond angle of 63.1° (Fig. 6). On the quintet surface, the $HIrCH_3^+$ intermediate retains the $^5A''$ state (C_s symmetry) and has a H–Ir–C bond angle of 144.2° (Fig. 6). In this molecule, both the Ir–H and Ir–C bond distances, 1.647 and 2.103 Å, respectively, are about 0.08 Å longer than those of IrH^+ ($^4\Sigma^-$), 1.570 Å, and $IrCH_3^+$ ($^4A_1$), 2.022 Å. This observation along with the Ir–C–H bond angles of ∼105° indicate that the methyl group is covalently bound to Ir in this state. The HIr^+–CH_3 bond energy is calculated to be 1.18 eV.

Continuing along the quintet surface, the $(H)_2IrCH_2^+$ intermediate is reached via ^{5}TS3, (Fig. 6), lying 1.43 eV above ground state reactants and 1.46 eV above the $HIrCH_3^+$ intermediate. The dihydride methylene intermediate lies 1.16 eV above the reactants and has Ir–H (1.604 Å) and Ir–C (2.009 Å) bond distances indicating covalent bonding interactions as they are similar to those of IrH^+ (1.570 Å) and $IrCH_3^+$ (2.022 Å). Clearly Ir cannot form a double bond with CH_2 in this species in order to maintain the high spin state. The dihydride methylene

Table 6
Theoretical structures of intermediates and transition states calculated at the B3LYP/HW+/6-311++G(3df,3p) level of theory[a]

Compound	State	*r*(Ir–H)	*r*(Ir–C)	*r*(C–H)	*r*(H–H)	∠IrCH	∠HCH	∠HIrC	∠HIrH	∠HIrCH
$IrCH_4^+$	$^3A''$	1.656	2.189	1.088(2), 1.097		97.5(2), 130.5	108.2(2), 115.0	36.6		0.0, ±121.7
	$^3A'$	1.683	2.242	1.086(2), 1.097		96.9(2), 131.3	108.2(2), 115.2	33.8		0.0, ±121.7
	$^3B_2$	1.928(2)	2.190	1.086(2), 1.154(2)	2.029	61.5(2), 122.6(2)	104.9(2), 114.8, 123.0	31.7(2)	63.5	±90.0, ±90.0
	$^3A_2$	2.062(2)	2.358	1.086(2), 1.122(2)	1.963	61.0(2), 122.2(2)	105.0(2), 115.6, 122.0	28.4(2)	56.8	±90.0, ±90.0
	$^5A''$	2.304, 2.460	2.782	1.088(2), 1.103, 1.112		53.6, 61.7, 123.3(2)	106.5(2), 107.8(2), 113.0, 115.4			±86.4, ±93.6, 180.0
	$^1A'$	1.671	2.223	1.088(2), 1.097		96.6(2), 130.9	109.0(2), 114.0	34.3		0.0, ±122.4
TS1	$^3A''$	1.638	2.169	1.089(2), 1.096, 1.350		98.0(2), 129.3	108.3(2), 114.9	38.5		0.0, ±121.7
	^1A	1.612	2.149	1.087, 1.093, 1.098		91.2, 105.5, 125.7	107.7, 112.2, 112.6	40.5		−103.0, 30.6, 143.5
	$^5A''$	1.568	3.229	1.080(2), 1.084		79.8, 102.6(2)	119.1(2), 119.4	63.1		±62.2, 180.00
$HIrCH_3^+$	$^3A''$	1.556	2.003	1.093, 1.095(2)		106.1(2), 107.8	111.2, 112.5(2)	100.8		±59.2, 180.0
	$^3A''$	1.554	2.007	1.085, 1.099(2)		102.5(2), 115.3	111.0, 112.3(2)	87.4		0.0, ±122.4
	$^3A'$	1.577	2.027	1.085, 1.096(2)		103.5(2), 113.0	110.6, 112.8(2)	94.0		0.0, ±122.3
	$^1A'$	1.555	1.991	1.096(2), 1.097		106.2(2), 109.2	109.8(2), 115.4	106.4		±61.7, 180.0
	$^5A''$	1.647	2.103	1.090, 1.095(2)		104.7(2), 107.5	111.9, 113.5(2)	144.2		0.0, ±121.1
TS2	$^5A''$	1.579, 1.662	2.050	1.090(2)	1.327	117.7(2),	119.9	92.6, 140.9	48.2	±102.2(2)
TS3	^1A	1.553	1.960	1.087, 1.095, 1.127		90.4, 112.3, 116.8	108.0, 112.6, 114.6	103.9		−56.2, 61.8, 171.6
	^3A	1.580, 1.621	1.871	1.084, 1.097	2.701	111.8, 128.1	120.0	61.4, 92.4	115.1	−122.8, −66.9, 50.6, 119.7
	^5A	1.591, 1.673	1.982	1.088, 1.093	2.827	113.1, 124.5	118.7	83.2, 137.9	120.0	−168.9, −95.0, 33.2, 62.9
$(H)_2IrCH_2^+$	$^1A'$	1.544(2)	1.818	1.089, 1.098	1.986	119.2, 123.8	117.0	90.5(2)	80.1	±40.0, ±140.0
	$^3A''$	1.580(2)	1.849	1.089, 1.093	2.660	116.3, 121.9	121.8	102.5(2)	114.6	±59.5, ±120.5
	$^5A''$	1.604(2)	2.009	1.092(2)	2.435	120.9(2)	118.3	130.6(2)	98.8	±90.0, ±90.0
TS4	^3A	1.563, 1.564	1.873	1.092, 1.097	2.171	115.2, 120.6	118.7	98.7, 103.4	88.0	−167.5, −77.5, −14.0, 76.0
	$^5A''$	1.614(2)	1.993	1.091, 1.092	2.194	117.9, 123.2	118.9	132.6(2)	85.6	±67.3, ±112.7
$(H_2)IrCH_2^+$	$^3A_2$	1.924(2)	1.879	1.092(2)	0.800	123.3(2)	113.5	168.0(2)	24.0	±0.0, ±180.0
	$^1A_1$	1.915(2)	1.873	1.093(2)	0.804	123.1(2)	113.7	167.9(2)	24.2	±0.0, ±180.0
	$^3B_2$	2.124(2)	1.873	1.093(2)	0.770	123.3(2)	113.4	169.6(2)	20.9	±90.0, ±90.0
	$^3B_1$	2.124(2)	1.869	1.093(2)	0.770	123.3(2)	113.4	169.6(2)	20.9	±90.0, ±90.0
	$^1A_1$	1.944(2)	1.835	1.095(2)	0.803	121.9(2)	116.1	168.1(2)	23.8	±0.0, ±180.0
	$^5A'$	1.944(2)	1.951	1.085, 1.094	0.803	114.4, 124.9	120.8	155.7(2)	23.9	±30.1, ±149.9

[a] Bond lengths are in Å. Bond angles are in degrees. Degeneracies are listed in parentheses.

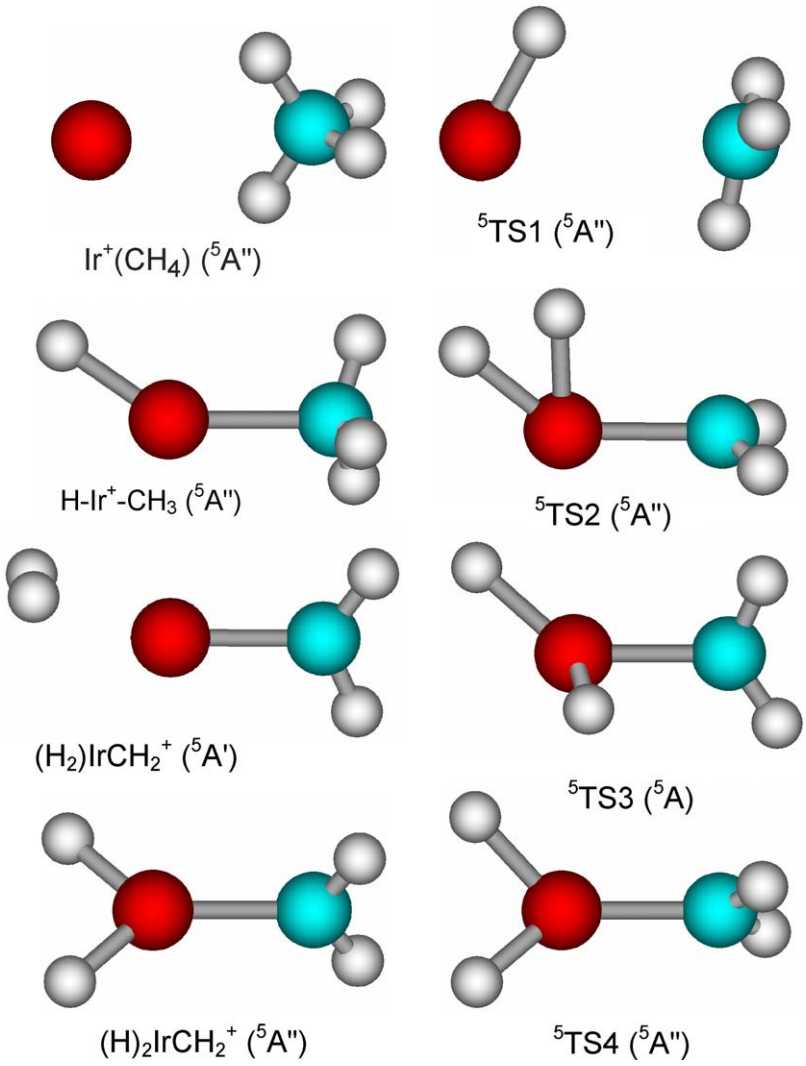

Fig. 6. Structures of several intermediates and transition states along the quintet surface of the [Ir, C, 4H]$^+$ system calculated at the B3LYP/HW+/6-311++G(3df,3p) level of theory.

intermediate converts to the $(H_2)IrCH_2^+$ intermediate via ^{5}TS4 (Fig. 6), which lies 0.005 eV *below* the dihydride after zero-point energies are included. The $(H_2)IrCH_2^+$ intermediate has C_s symmetry with a H_2 bond distance of 0.803 Å, comparable to that of H_2, 0.742 Å. The geometry of the $IrCH_2^+$ part of the molecule is similar to that for $IrCH_2^+$ (^{5}A′) (Fig. 6). Overall, this is consistent with the weak H_2–$IrCH_2^+$ bond energy, calculated to be only 0.41 eV relative to the $IrCH_2^+$ (^{5}A′) + H_2 asymptote.

An alternative pathway for transition between the $HIrCH_3^+$ and $(H_2)IrCH_2^+$ intermediates was also located and involves the four-centered transition state ^{5}TS2. This transition state lies 1.38 eV above $HIrCH_3^+$ and 1.35 eV above the ground-state reactants. The transition state for the sequential α-H migration pathway (^{5}TS3) is slightly higher in energy (by 0.07 eV) than the four-centered pathway of ^{5}TS2 (Fig. 5).

5.2. Triplet surface

The interaction of methane with the triplet state of Ir^+ (^{3}F, $5d^8$) leads initially to the formation of an $Ir^+(CH_4)$ adduct (^{3}A″) in which the methane molecule distorts severely as the C–H bond begins to break (Fig. 7). Previous work constrained their calculations to C_{2v} symmetry, finding either a $^3B_2$ [25] or $^3A_2$ [26] state. These intermediates were calculated to lie 0.87 and 0.26 eV below the Ir^+ (^{5}F) + CH_4 reactants, whereas our intermediate is more stable, 1.27 eV below the ground-state reactants. Upon further reduction of the Ir–H bond distance, the system passes over a transition state, ^{3}TS1 (^{3}A″) with an HIrC bond angle of 38.5°, leading to the insertion intermediate H–Ir^+–CH_3. Once zero-point energies are included, the energy of ^{3}TS1 is lower than the $Ir^+(CH_4)$ (^{3}A″) intermediate, Fig. 7, indicating that oxidative addition of the C–H bond of methane to Ir^+ (^{3}F) is spontaneous. These closely spaced relative energies were also found in the work of POG [25], where the ^{3}A′ transition state has an energy 0.87 eV below the Ir^+ (^{5}F) + CH_4 reactants, the same energy as their triplet $Ir^+(CH_4)$ intermediate. In contrast, MM identify a triplet transition state lying 0.17 eV below the Ir^+ (^{5}F) + CH_4 reactants, 0.09 eV above their $Ir^+(CH_4)$ intermediate.

The triplet $HIrCH_3^+$ intermediate lies below the comparable species having quintet and singlet spin, as would be expected

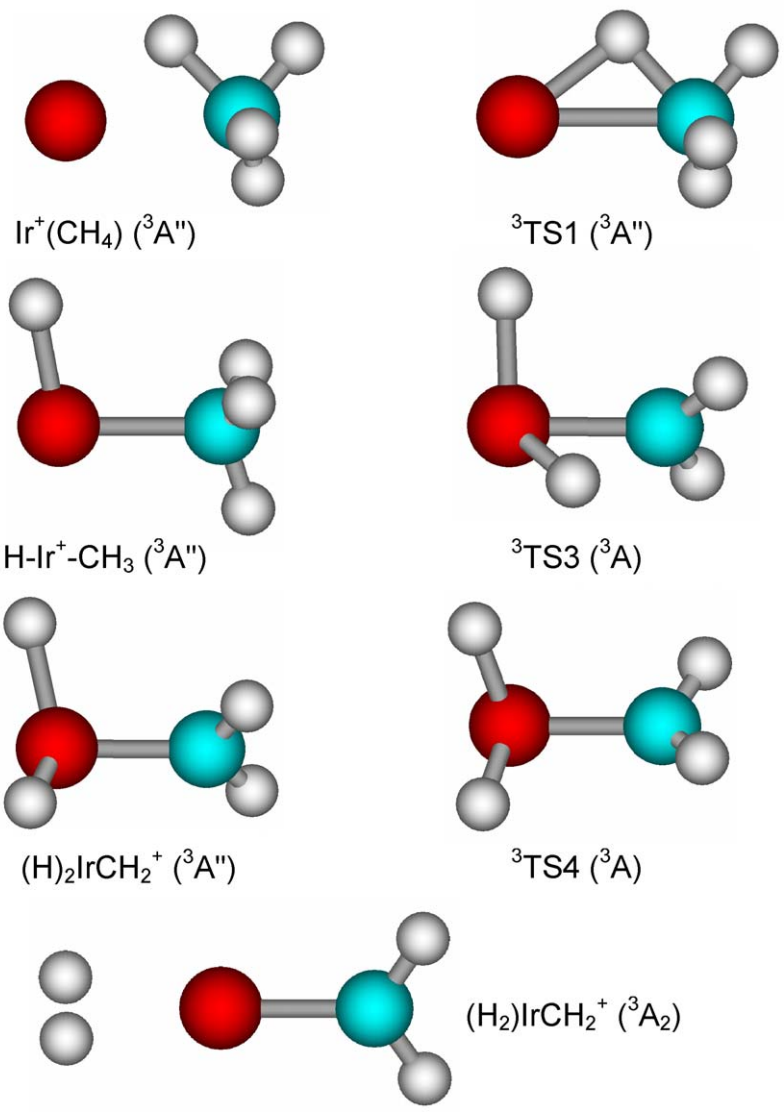

Fig. 7. Structures of several intermediates and transition states along the triplet surface of the [Ir, C, 4H]$^+$ system calculated at the B3LYP/HW+/6-311++G(3df,3p) level of theory.

according to Hund's rules for a species forming two covalent bonds, thus leaving six electrons in four nonbonding orbitals. This $^3A''$ intermediate has C_s symmetry and a HIrCH dihedral angle of 180°. Upon rotation to a HIrCH dihedral angle of 0°, there is another stable $^3A''$ state lying 0.04 eV higher in energy. ($A\,^3A'$ state was also found with an excitation energy of 0.40 eV.) Both POG and MM identify this same $HIrCH_3^+$ ($^3A''$) state, and calculate relative energies of 1.74 and 0.64 eV, respectively, below the reactants, compared with our value of 1.95 eV.

From $HIrCH_3^+$ ($^3A''$), a $(H)_2IrCH_2^+$ ($^3A''$) dihydride intermediate is reached via ^{3}TS3 (Fig. 7). This transition state lies 1.21 eV above $HIrCH_3^+$ ($^3A''$) and 0.25 eV higher in energy than $(H)_2IrCH_2^+$ ($^3A''$). Note that the two Ir–H (both 1.580 Å) and Ir–C (1.849 Å) bonds length of $(H)_2IrCH_2^+$ are only slightly longer than those of IrH^+ ($^4\Sigma^-$) (1.570 Å) and $IrCH_2^+$ ($^3A_2$) (1.836 Å), indicating the formation of strong covalent bonds. The triplet dihydride is calculated to lie 1.00 eV below the ground state reactants, somewhat more stable than the results of POG, which place this species at 0.48 eV below reactants. In contrast, the work of MM found a $(H)_2IrCH_2^+$ (^3A) state lying 1.33 eV *above* Ir^+ (^5F) + CH_4. Several attempts to locate a four-centered ^{3}TS2 transition state always collapsed directly to ^{3}TS3. It might also be noted that neither POG nor MM identified such a four-centered transition state on the triplet surface either.

The triplet dihydride intermediate begins to eliminate dihydrogen by passing over ^{3}TS4, which lies only 0.16 eV higher in energy than the dihydride intermediate. The ground $(H_2)IrCH_2^+$ ($^3A_2$) intermediate is planar and has an H_2 bond distance of 0.800 Å compared to free H_2 at 0.742 Å. It lies 1.08 eV below the ground state reactants, whereas two excited states of $(H_2)IrCH_2^+$, $^3B_2$ and $^3B_1$, lie 0.65 and 0.69 eV higher in energy, respectively. POG identify the same $(H_2)IrCH_2^+$ ($^3A_2$) intermediate, and calculate it has an energy of 0.91 eV below the reactants. MM find a $(H_2)IrCH_2^+$ ($^3A_2$) state with an energy 0.12 eV above Ir^+ (^5F) + CH_4. The $(H_2)IrCH_2^+$ ($^3A_2$) intermediate then dissociates to H_2 and $IrCH_2^+$ ($^3A_2$), which lies 0.55 eV below

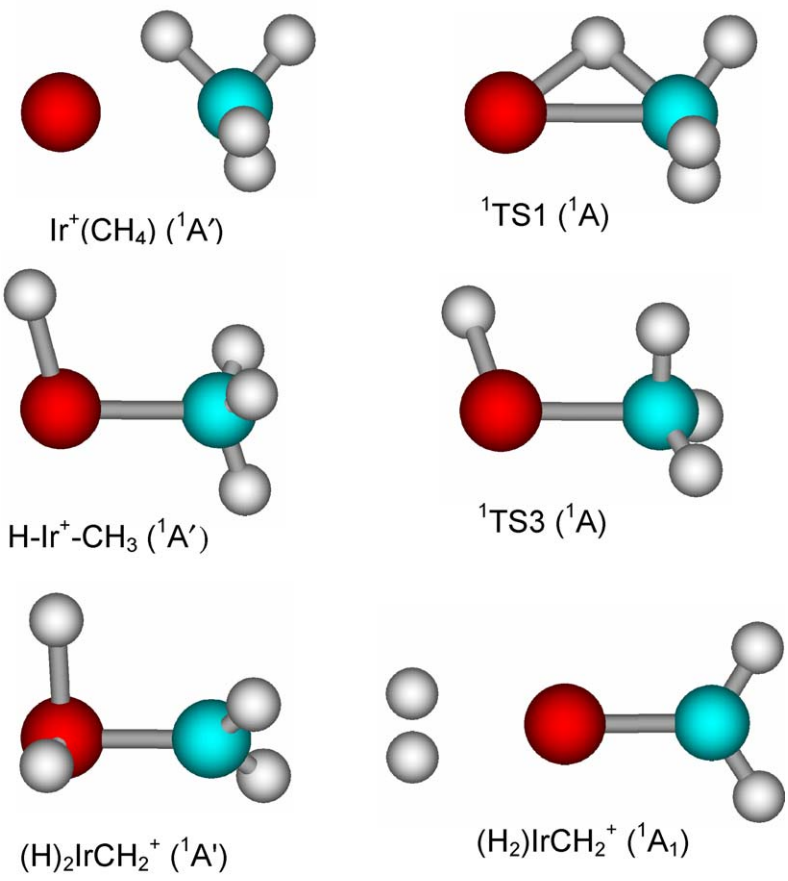

Fig. 8. Structures of several intermediates and transition states along the singlet surface of the [Ir, C, 4H]$^+$ system calculated at the B3LYP/HW+/6-311++G(3df,3p) level of theory.

the ground state reactants. POG finds an exothermicity for this reaction of 0.13 eV, whereas MM find the reaction is endothermic by 0.50 eV, although higher level calculations performed only for the $IrCH_2^+$ species reduce this to an exothermicity of 0.09 eV. These various values can be favorably compared with the experimental exothermicity of 0.21 ± 0.03 eV.

5.3. Singlet surface

The interaction of methane with the singlet state of Ir^+ (^{1}D/G, $5d^8$) leads initially to the formation of a $Ir^+(CH_4)$ (^{1}A′) adduct in which the methane molecule is strongly distorted as the C–H bond is activated (Fig. 8). (This intermediate was found only when using Int = ultrafine and opt = tight options in the Gaussian geometry optimization.) MM identified this species as a $^1A_1$ state lying 0.68 eV above Ir^+ (^{5}F) + CH_4, compared to our relative energy of 0.18 eV. Upon further reduction of the Ir–H bond distance, the system passes over a transition state, ^{1}TS1, having a HIrC bond angle of 40.5° and leading to the insertion intermediate H–Ir^+–CH_3 (^{1}A′). As for the analogous triplet species, once zero-point energies are included, the energy of ^{1}TS1 is lower than $Ir^+(CH_4)$, Fig. 5, indicating that C–H bond activation is spontaneous. We calculate that ^{1}TS1 and $HIrCH_3^+$ (^{1}A′) lie 0.13 eV above and 0.88 eV below, respectively, the ground state reactants, whereas MM find these species lie 1.10 and 0.40 eV, respectively, above the Ir^+ (^{5}F) + CH_4 reactants.

Continuing along the singlet surface, the system passes over ^{1}TS3 to form the global minimum of all potential energy surfaces, the $(H)_2IrCH_2^+$ dihydride methylene iridium cation (Fig. 8). ^{1}TS3 lies 1.68 eV higher in energy than the $(H)_2IrCH_2^+$ (^{1}A′) intermediate, but lies 0.010 eV *below* the $HIrCH_3^+$ (^{1}A′) intermediate once zero-point energies are included. Thus, interaction of Ir^+ (^{1}D/G) with methane spontaneously forms the dihydride methylene, which lies 2.57 eV below the ground state reactants. A singlet spin state is anticipated for a molecule with four covalent bonds to Ir^+ (Fig. 8). Indeed, Ir–H (1.544 Å) and Ir–C (1.818 Å) bond distances in this intermediate indicate covalent bonding interactions as they are similar to those of IrH^+ ($^4\Sigma^-$) (1.57 Å) and $IrCH_2^+$ ($^3A_2$) (1.84 Å). In POG's work, they also identified the $(H)_2IrCH_2^+$ (^{1}A′) species as the global minimum on the potential energy surfaces with an energy 2.73 eV below Ir^+ (^{5}F) + CH_4, similar to our results, and well below the energy of 0.96 eV found in the work of MM. The ^{1}TS3 transition state was also identified by MM with an energy of 0.490 eV above Ir^+ (^{5}F) + CH_4. Several attempts to locate a four-centered ^{1}TS2 transition state always collapsed directly to ^{1}TS3. Again, it can be noted that neither POG nor MM identified such a four-centered transition state on the singlet surface.

From the dihydride intermediate, the reaction can proceed on the singlet surface to eliminate dihydrogen. No transition state between $(H)_2IrCH_2^+$ (^{1}A′) and $(H_2)IrCH_2^+$ ($^1A_1$) could be found even though extensive searches were conducted. We

did identify two $(H_2)IrCH_2^+$ ($^1A_1$) intermediates, both having a planar structure and H_2 bond distances of 0.80 Å compared to free H_2 at 0.74 Å. They are distinguished by different Ir–H and Ir–C bond lengths, Table 6. It is believed that the lower-lying state is largely an artifact as it is heavily spin contaminated, $s(s+1) = 0.95$, with a structure and energy very similar to that of the $^3A_2$ ground state of this species. In contrast, the higher lying $^1A_1$ has an imaginary frequency (72 cm^{-1}) largely corresponding to the movement of the H_2 to a nonplanar geometry, i.e., bending of the C–Ir–(H_2) angle. Once this bending occurs, the H_2 bond is rapidly activated, forming the dihydride intermediate. This characteristic is consistent with our inability to locate a transition state between the dihydride and $(H_2)IrCH_2^+$ ($^1A_1$) and demonstrates that activation of H_2 by $IrCH_2^+$ ($^1A_1$) is barrierless and spontaneous. A further indication that the lower $^1A_1$ state is anomalous compares the bond energies for loss of H_2 from the various $(H_2)IrCH_2^+$ species. On the quintet and triplet surfaces, these bond energies are 0.41 and 0.53 eV, respectively, comparable to the 0.54 eV calculated for the upper $^1A_1$ state, but well below the 1.08 eV found for the lower, spin-contaminated $^1A_1$ state. In the studies of POG and MM, the $(H_2)IrCH_2^+$ ($^1A_1$) intermediate was calculated to have energies of 0.52 eV below and 0.78 eV above, respectively, Ir^+ (^5F) + CH_4. The former is clearly consistent with the present results.

Viewed more globally, we find our potential energy surface (Fig. 5) is qualitatively consistent in many respects with the previously reported PESs of POG and MM [25,26], as they all contain the same intermediates and transition states. A more detailed comparison shows that the results of POG [25] are quantitatively similar to the present results, with energetic differences of only 0.3 ± 0.2 eV for 10 different intermediates, transition states, and products along the singlet, triplet, and quintet surfaces. The present calculations appear to have been more successful in characterizing the triplet $(H)_2IrCH_2^+$ intermediate and adjoining ^{3}TS3 and ^{3}TS4 transition states than the approach of POG. In contrast, the results of MM [26] lie well above the present results by an average of 1.1 ± 0.2 eV for 11 different intermediates, transition states, and products along the singlet, triplet, and quintet surfaces. This average excludes results for the singlet and triplet dihydride intermediates, $(H)_2IrCH_2^+$, which differ from the present calculations by 1.6 eV for the singlet and 2.3 eV for the triplet. Part of these discrepancies appear to be the result of not using polarization functions on the Ir atom, because the Ir^+–CH_2 BDE calculated by MM increases by 0.6 eV when these are included. Overall, the quantitative character of the surfaces calculated by MM is not in good agreement with the present results, those of POG, or the experimental results.

6. Discussion

σ-Bond activation by atomic metal ions can be explained using a simple donor–acceptor model. Such reactions require electronic configurations in which there is an empty acceptor orbital on the metal ion into which the electrons of a bond to be broken are donated. Concomitantly, metal electrons in orbitals having π-symmetry back donate into the antibonding orbital of the bond to be broken. If the acceptor orbital is occupied, a repulsive interaction can result leading to inefficient reaction either by more direct abstraction pathways or by introduction of a barrier to the reaction. In our previous studies [9–16], the activation of methane by atomic metal ions was explained by this simple donor–acceptor model, which leads to an oxidative addition mechanism [4]. In such a mechanism, oxidative addition of a C–H bond to M^+ forms a H–M^+–CH_3 intermediate. Products can be formed by the reductive elimination of H_2 at low energies and by further dehydrogenation of primary products at still higher energies. For first-row transition metal ions [4], the reductive elimination process proceeds through a four-centered transition state from the H–M^+–CH_3 intermediate to a $(H_2)MCH_2^+$ intermediate in which a hydrogen molecule is electrostatically bound to the MCH_2^+ species. This latter intermediate then decomposes by expulsion of H_2. However, for the reaction of Ir^+ with methane, the calculated potential energy surfaces of POG and MM [25,26], as confirmed by the calculations performed here (Fig. 5), illustrate a different reaction mechanism involving a dihydride methylene intermediate.

6.1. Mechanism for dehydrogenation of Ir^+ with methane

On the quintet surface, $^5TS_1$, $^5TS_2$, $^5TS_3$, and $^5TS_4$ are much higher in energy than the $IrCH_2^+$ product formed in an exothermic process. Because Ir^+ (^5F, $6s^15d^7$) has no empty valence orbitals, the simple donor–acceptor process is restricted, leading to the high barrier for ^{5}TS1. The energies of ^{5}TS2, ^{5}TS3, and ^{5}TS4 are even higher because the high spin does not allow formation of the several covalent bonds needed to stabilize these three transition states. Thus, at low energies, reaction of Ir^+ (^5F) with methane must occur by coupling to the triplet surface where oxidative addition of CH_4 to Ir^+ produces a triplet hydrido methyl iridium cation intermediate, H–Ir^+–CH_3 ($^3A''$). On the triplet surface, the empty *s* orbital of Ir^+(^3F, $5d^8$) acts as an efficient acceptor orbital, and a doubly occupied 5dπ orbital can provide an efficient donor orbital. This leads naturally to an intermediate in which Ir^+ forms two covalent bonds using 6s5d hybrids.

From H–Ir^+–CH_3 ($^3A''$), the activation of a second C–H bond (α-H transfer) can lead to formation of a dihydride methylene iridium cation intermediate, $(H)_2IrCH_2^+$ ($^3A''$). Reductive elimination of dihydrogen then forms the $(H_2)IrCH_2^+$ ($^3A_2$) intermediate that easily loses dihydrogen to form the ground state $IrCH_2^+$ ($^3A_2$) + H_2 products. Note that ^{3}TS1, ^{3}TS3, and ^{3}TS4 all lie below the energy of the $IrCH_2^+$ ($^3A_2$) + H_2 products, such that the dehydrogenation reaction is barrierless along the triplet surface. This is similar to the mechanism found for the dehydrogenation reactions of methane with Pt^+ (^2D), although here the reaction remains on a doublet surface throughout [19,65–67], and with W^+ (^6D), which must couple to the quartet and doublet spin surfaces to form a dihydride intermediate. This pathway is different from those of the first-row transition metal ions, which involve a four-centered transition state, TS2, that bypasses the dihydride intermediate and is found here along the high spin quintet surface.

However, the global minimum on the potential energy surface is $(H)_2IrCH_2^+$ ($^1A'$). This suggests that there could be another

pathway available for dehydrogenation that involves coupling between the triplet and singlet surfaces. Once the H–Ir^+–CH_3 ($^3A''$) intermediate is formed, it can cross over to the singlet surface forming the $(H)_2IrCH_2^+$ ($^1A'$) intermediate. Reductive 1,1-elimination of dihydrogen on the singlet surface could again couple back to the triplet surface to form $(H_2)IrCH_2^+$($^3A_2$), followed by reductive elimination of dihydrogen to yield $IrCH_2^+$ ($^3A_2$) + H_2. This type of mechanism is also available for both W^+ (^6D) and Re^+ (^7S) reacting with methane, where multiple spin changes are also required [20,21].

6.2. Mechanism for higher energy products

As the energy available increases above about 1.6 eV, IrH^+ and $IrCH_3^+$ products are formed by simple bond cleavages of the H–Ir^+–CH_3 intermediate. These processes, in particular formation of $IrH^+ + CH_3$, deplete the population of this intermediate such that the cross section for the dehydrogenation process declines commensurately. Because formation of $IrCH_2^+ + H_2$ is thermodynamically preferred by about 1.8 eV (Table 2), this competition indicates that formation of $IrH^+ + CH_3$ must be preferred kinetically. This is consistent with a simple bond cleavage of HIr^+–CH_3 at elevated kinetic energies, whereas the elimination of H_2 occurs via the more restricted pathway discussed above.

In the reaction of Ir^+ with CH_4 (CD_4), the IrH^+ (IrD^+) cross section is dominant at energies above 3 eV (Fig. 1). This is typical behavior for the reaction of bare metal ions with hydrogen-containing polyatomic molecules [4,9,16,18–21]. The observation that the $IrH^+ + CH_3$ ($IrD^+ + CD_3$) channel dominates the nearly isoenergetic $IrCH_3^+ + H$ ($IrCD_3^+ + D$) channel (Table 1) is largely a result of angular momentum constraints [9–11,18]. Briefly, because the $IrCH_3^+ + H$ ($IrCD_3^+ + D$) channel has a reduced mass of 1.0 (2.0) amu, much smaller than that of the reacants, 14.8 (18.1) amu, it can only be formed by the reactants that come together with smaller orbital angular momenta, i.e., at small impact parameters. In contrast, the $IrH^+ + CH_3$ ($IrD^+ + CD_3$) channel has a reduced mass of 13.9 (16.5) amu, close to that of the reactants, such that most impact parameters leading to strong interactions between the Ir^+ and methane can form these products and still conserve angular momentum. Although the branching ratio of $\sigma(IrD^+)/\sigma(IrCD_3^+)$ ranges from about 20 to 100 from threshold to 6 eV, the magnitude of the $IrCD_3^+$ product is also limited by decomposition to form $IrCD^+$. Thus, the $\sigma(IrD^+)/[\sigma(IrCD_3^+) + \sigma(IrCD^+)]$ branching ratio changes from about 20 to 4 over the energy range of 2–5 eV, which is consistent with the range of 4–20 suggested as appropriate for a statistical mechanism associated with a long-lived intermediate [18,42].

At higher energies, IrC^+ and $IrCH^+$ products are formed by dehydrogenation of the primary products, $IrCH_2^+$ and $IrCH_3^+$, respectively. The thermochemistry determined above (Table 2) shows that these dehydrogenations require 1.68 ± 0.06 and 0.93 ± 0.29 eV, respectively. In addition, H atom loss from $IrCH_3^+$, which requires 3.04 ± 0.18 eV, leads to the second feature in the $IrCH_2^+$ cross-section (Fig. 1). This process is observed because the simple bond cleavage is kinetically more favorable at high energies than the more complex dehydrogenation process. Comparable observations have been made for second-row [11,16,17,68,69] and third-row (W^+, Re^+ and Pt^+) metal systems [19–21].

The highest energy process observed experimentally is formation of $IrH_2^+ + CH_2$. It seems unlikely that this species is formed from the $(H_2)IrCH_2^+$ intermediate, because H_2 is bound to Ir^+ much less strongly than methylene (BDEs of $>0.61 \pm 0.07$ versus 4.92 ± 0.03 eV, respectively). Further, cleavage of the electrostatic (H_2)–$IrCH_2^+$ bond is a dynamically much more favorable process than breaking the covalent $(H_2)Ir^+$–CH_2 bond. However, CH_2 could be lost from the $(H)_2IrCH_2^+$ intermediate to produce the H–Ir^+–H dihydride. CH_2 loss is more favorable dynamically because of the angular momentum considerations discussed above and because it is a simple bond cleavage whereas H_2 loss involves the recombination of two H atoms over a tight transition state. Thus, the product IrH_2^+ in this system provides evidence for a reaction pathway involving the $(H)_2IrCH_2^+$ intermediate. A similar result was also found for Pt^+ reacting with methane, where PtH_2^+ is detected [19], whereas the analogous product was not observed for W^+ and Re^+ reacting with methane [20,21].

6.3. Mechanism for the reverse reaction, $IrCH_2^+ + H_2$

We can also understand the reverse reaction of $IrCH_2^+ + H_2$ (D_2) through the potential energy surface of Fig. 5. Scrambling of the isotopes to form $IrCHD^+$ and $IrCD_2^+$ cannot occur from the intermediates analogous to $(H_2)IrCH_2^+$ and $(H)_2IrCH_2^+$, but can only proceed if the H–Ir^+–CH_3 intermediate is involved. Addition of D_2 to $IrCH_2^+$ ($^3A_2$) would form a triplet D–Ir^+–CH_2D intermediate, which can reductively eliminate either D_2 to return to reactants or HD to form the dominant $IrCHD^+$ product, Fig. 3, via a (H)(D)$IrCHD^+$ intermediate which could be either the singlet or triplet species. Competing with this is the more energetic loss of CH_2D_2 to yield Ir^+. At higher energies, the D–Ir^+–CH_2D intermediate can decompose to form $IrCH_2D^+ + H$ and $IrD^+ + CHD_2$. (Note that the iridium methyl cation product is much more abundant relative to the iridium hydride. This is because the angular momentum constraints discussed above are no longer applicable because the $IrCH_2^+ + D_2$ reactants have a much smaller reduced mass.) Alternatively, the (H)(D)$IrCHD^+$ intermediate can form H–Ir^+–CHD_2 from which H_2 or HD can be eliminated to yield $IrCHD^+$ or $IrCD_2^+$ at low energies, and $IrCHD_2^+ + H$ and $IrH^+ + CHD_2$ at higher energies. However, because (H)(D)$IrCHD^+$ intermediate must be formed prior to the rearrangement that yields the H–Ir^+–CHD_2 intermediate, these latter three ionic products are less abundant than the analogous species, $IrCHD^+$, $IrCH_2D^+$, and IrD^+, formed from the D–Ir^+–CH_2D intermediate. As the available energy increases, the need for multiple access to the hydrido methyl intermediate can limit the extent of exchange such that H_2 loss becomes less favored. Indeed, this can explain why the branching ratio between HD and H_2 loss increasingly favors HD loss as the kinetic energy is increased (the $IrCHD^+$ cross section is larger than that of $IrCD_2^+$ by a factor of about 4 at the lowest energies, and the ratio increases to about 12 by 1 eV). This also

reflects the shorter lifetime of the intermediate at these higher energies.

The acceptor–donor concept can also be used to understand the activation of dihydrogen by $IrCH_2^+$ and this provides more insight into the dehydrogenation reaction (5) as well. On the triplet surface, the $^3A_2$ ground state of $IrCH_2^+$ has an electron configuration of $(1a_1)^2(1b_1)^2(1b_2)^2(1a_2)^1(2a_1)^2(3a_1)^1$. The most likely acceptor orbital is the partialy occupied $3a_1$ orbital, largely a 6s orbital on Ir with some 6s5d hybridization. The occupation of the $3a_1$ acceptor orbital means that the Ir–C π bond becomes partially disrupted as the $(H)_2IrCH_2^+$ intermediate is formed, such that the triplet dihydride is a relatively high-energy species compared to the $H–Ir^+–CH_3$ intermediate. The donor orbital on $IrCH_2^+$ that interacts with the antibonding orbital of H_2 is the doubly occupied $2a_1$ nonbonding orbital, essentially $5d(x^2 - y^2)$. These donor–acceptor interactions lead to the oxidative addition of H_2 to the Ir^+ center of $IrCH_2^+$ via a three-centered transition state (^{3}TS3). On the singlet surface, the $^1A_1$ excited state of $IrCH_2^+$ has an electron configuration of $(1a_1)^2(1b_1)^2(1b_2)^2(1a_2)^2(2a_1)^2$. Now, the $3a_1$ acceptor orbital is empty and again the donor orbital is the doubly occupied $2a_1$ nonbonding orbital. These favorable donor–acceptor interactions lead to the oxidative addition of H_2 to the Ir^+ center of $IrCH_2^+$ ($^1A_1$) via a pathway with no transition state and lead directly to the $(H)_2IrCH_2^+$ ($^1A'$) intermediate, the global minimum on the potential energy surface. This contrasts with the transition state for the comparable reactions involving first-row and second-row transition metal systems, where H_2 adds across the $M^+–CH_2$ bond via a four-centered transition state (like ^{5}TS2, Fig. 6), largely because only high spin surfaces are energetically accessible.

6.4. Reactivity difference between Co^+, Rh^+, and Ir^+ systems

Ir^+ exhibits greater reactivity toward methane than any ions of the first-row and second-row metals [4,9,17,18]. To characterize these differences, we explicitly compare the present results with comparable studies of the kinetic energy dependence of the reaction of CH_4 with corresponding first-row and second-row ions, Co^+ and Rh^+ [11,14]. The differences in reaction behavior between these three metal systems can be summarized succinctly. First, the bonding of Ir^+ with H and CH_x ($x = 0–3$) is stronger than that of Co^+ and Rh^+, as shown in Fig. 4. Second, in contrast to the behavior observed here, the dehydrogenation reactions are endothermic for the Co^+ and Rh^+ systems. In addition, there is a barrier in excess of the endothermicity for the Co^+ system. Third, the iridium dihydride cation is observed here but no MH_2^+ is observed in the Co^+ or Rh^+ systems.

All of these differences can be understood on the basis of promotion energy and sd hybridization. (1) For single bond products, MH^+ and MCH_3^+, the ground state of Ir^+ is $5d^76s^1$, such that it can form a covalent bond without any promotion energy. For Co^+ and Rh^+, the ground states are $3d^8$ and $4d^8$, respectively, such that they need promotion to form a single covalent bond. For Co^+, this promotion is to a $3d^74s^1$ state (mixtures of 50% ^{5}F and 50% ^{3}F), which costs only 0.82 eV [70]. For Rh^+, promotion to the $4d^75s^1$ (mixtures of 50% ^{5}F and 50% ^{3}F) is high (2.63 eV) [70], such that RhH^+ and $RhCH_3^+$ are formed by a covalent bond between the 4dσ orbital of ground state Rh^+ and H(^{2}S) or $CH_3(^2A_1)$, where the promotion energy is much smaller, 0.29 eV [4,38,70], but the bond is weaker. (2) For multiple bond products, MCH_2^+, MCH^+ and MC^+, sd hybridization is required to form the multiple bonds. The ground state of Ir^+ is $5d^76s^1$, such that it can form multiple bonds without any promotion energy, and also the similar size of the s and d orbitals (6s/5d ratio is 1.65) makes sd hybridization efficient [58]. For Co^+ and Rh^+, the ground states are $3d^8$ and $4d^8$, respectively, such that they need promotion to $3d^74s^1$ and $4d^75s^1$ configuration to form multiple bonds. The sd hybridization is less efficient for Co^+ than Ir^+ and Rh^+ because the 4s orbital of Co^+ is 2.58 times the size of the 3d orbitals, where Rh^+ is intermediate with a ratio of 1.97:1 for 5s/4d [58]. These factors determine that for single bond MH^+ and MCH_3^+, Ir^+ has the strongest BDEs, whereas Rh^+ has the weakest BDEs. For multiple bonds, Ir^+ still has the strongest BDEs, whereas Co^+ has the weakest BDEs. Such thermodynamic differences stabilize the various transition states and intermediates along the dehydrogenation pathway for Ir^+, enabling this reaction to occur efficiently at room temperature. In the cobalt and rhodium systems, the inability to form multiple bonds means that the $(H)_2MCH_2^+$ intermediate is not stable, thus a relatively high energy four-centered transition state is needed for the dehydrogenation process [11,14,26]. Similarly, efficient dehydrogenation of primary products to form IrC^+ and $IrCH^+$ are consequences of the enhanced thermodynamic stability afforded by the accessibility of the s^1d^7 configuration and efficient sd hybridization.

7. Conclusions

Ground-state Ir^+ ions are found to be highly reactive with methane over a wide range of kinetic energies. At low energies, dehydrogenation is efficient, exothermic, and a dominant process. At high energies, the dominant process is formation of $IrH^+ + CH_3$. This channel is favored over the nearly isoenergetic $IrCH_3^+ + H$ channel because of angular momentum constraints. At higher energies, the $IrCH_2^+$ and $IrCH_3^+$ products decompose by dehydrogenation to form IrC^+ and $IrCH^+$, respectively, and at still higher energies by H atom loss to yield $IrCH^+$ and $IrCH_2^+$. The observation of IrH_2^+, which finds no analogy in the product spectrum for first-row and second-row transition metal systems, suggests involvement of a dihydride intermediate, providing evidence for the reaction pathway involving the $(H)_2IrCH_2^+$ intermediate.

Analyses of the kinetic energy dependences of the reaction cross sections provide the BDEs of $Ir^+–CH_3$, $Ir^+–CH$, and $Ir^+–C$. The BDE for $Ir^+–CH_2$ is determined from a measurement of the equilibrium constant for the forward and reverse dehydrogenation reactions. These experimental bond energies are stronger than the corresponding ones of the first-row and second-row transition metals, which is attributed to the accessibility of the s^1d^7 electronic configuration and effective sd hybridization, a consequence of relativistic effects. Our experimental BDEs are

found to be in reasonable agreement with ab initio calculations performed here and in the literature (Table 2 and Fig. 4).

Calculations are also used to provide a detailed potential energy surface for the $IrCH_4^+$ system. As found previously [25,26], this potential energy surface shows that the reaction of $Ir^+(^5F)$ with methane proceeds via the oxidative addition of one C–H bond to yield a hydrido-methyl iridium intermediate, H–Ir^+–CH_3 ($^3A''$). IrH^+ and $IrCH_3^+$ can be formed by simple bond cleavages from this intermediate. The activation of a second C–H bond proceeds through a three-centered transition state involving migration of an H-atom from C to Ir^+ to form a $(H)_2IrCH_2^+$ ($^1A'$ or $^3A''$) intermediate, where $(H)_2IrCH_2^+$ ($^1A'$) is the global minimum. Reductive elimination of H_2 forms the electrostatic complex, $(H_2)IrCH_2^+$ ($^3A_2$), from which H_2 is eliminated to form the metal carbene complex, $IrCH_2^+(^3A_2) + H_2$. IrH_2^+ is produced by expulsion of CH_2 from $(H)_2IrCH_2^+$. IrC^+ and $IrCH^+$ are formed by the dehydrogenation of the Ir^+–CH_2 and Ir^+–CH_3 primary product, respectively. Overall, dehydrogenation of methane by Ir^+ appears to have two available pathways. One pathway requires only a single spin change: Ir^+ (^5F) + CH_4 ($^1A_1$) → H–Ir^+–CH_3 ($^3A''$) → $(H)_2IrCH_2^+$ ($^3A''$) → $(H_2)IrCH_2^+$ ($^3A_2$) → $IrCH_2^+$ ($^3A_2$) + H_2 ($^1\Sigma^+$). The other pathway requires three spin changes along the lowest adiabatic energy path available: Ir^+ (^5F) + CH_4 ($^1A_1$) → H–Ir^+–CH_3 ($^3A''$) → $(H)_2IrCH_2^+$ ($^1A'$) → $(H_2)IrCH_2^+$ ($^3A_2$) → $IrCH_2^+$ ($^3A_2$) + H_2 ($^1\Sigma^+$). Despite the need to change spin, the dehydrogenation reaction is found to occur with high efficiency (70–100%), suggesting that spin conservation is not an impediment for reaction of this heavy metal system. This conclusion is similar to that drawn in the $Re^+ + CH_4$ system, where the reaction efficiency is $86 \pm 10\%$ even though three spin changes are required for dehydrogenation [20].

Acknowledgment

This work is supported by the National Science Foundation, Grant CHE-0451477.

References

[1] (a) A.H. Janowicz, R.G. Bergman, J. Am. Chem. Soc. 104 (1982) 352;
(b) J.K. Hoyano, W.A.G. Graham, J. Am. Chem. Soc. 104 (1982) 3723;
(c) J.K. Hoyano, A.D. McMaster, W.A.G. Graham, J. Am. Chem. Soc. 105 (1983) 7190;
(d) J.M. Buchanan, J.M. Stryker, R.G. Bergman, J. Am. Chem. Soc. 108 (1986) 1537;
(e) T. Foo, R.G. Bergman, Organometallics 11 (1992) 1801;
(f) T. Foo, R.G. Bergman, Organometallics 11 (1992) 1811.
[2] K.K. Irikura, J.L. Beauchamp, J. Phys. Chem. 95 (1991) 8344.
[3] J. Allison, Prog. Inorg. Chem. 34 (1986) 627;
R.R. Squires, Chem. Rev. 87 (1987) 623;
D.H. Russell (Ed.), Gas-Phase Inorganic Chemistry, Plenum, New York, 1989;
K. Eller, H. Schwarz, Chem. Rev. 91 (1991) 1121.
[4] For reviews;
(a) P.B. Armentrout, B.L. Kickel, in: B.S. Freiser (Ed.), Organometallic Ion Chemistry, Kluwer, Dordrecht, 1996, p. 1;
(b) P.B. Armentrout, in: J.M. Brown, P. Hofmann (Eds.), Topics in Organometallic Chemistry, vol. 4-I, Springer-Verlag, Berlin, 1999, p. 1.
[5] R.H. Crabtree, The Organometallic Chemistry of the Transition Metals, 2nd ed., Wiley, New York, 1994.
[6] G.A. Somorjai, Introduction to Surface Chemistry and Catalysis, Wiley, New York, 1994.
[7] P.B. Armentrout, M.R. Sievers, J. Phys. Chem. A 107 (2003) 4396.
[8] F. Liu, X.-G. Zhang, P.B. Armentrout, Phys. Chem. Chem. Phys. 7 (2005) 1054.
[9] N. Aristov, P.B. Armentrout, J. Phys. Chem. 91 (1987) 6178.
[10] L.S. Sunderlin, P.B. Armentrout, J. Phys. Chem. 92 (1988) 1209.
[11] Y.-M. Chen, P.B. Armentrout, J. Phys. Chem. 99 (1995) 10775.
[12] R.H. Schultz, J.L. Elkind, P.B. Armentrout, J. Am. Chem. Soc. 110 (1988) 411.
[13] R. Georgiadis, P.B. Armentrout, J. Phys. Chem. 92 (1988) 7067.
[14] C.L. Haynes, Y.-M. Chen, P.B. Armentrout, J. Phys. Chem. 99 (1995) 9110.
[15] C.L. Haynes, Y.-M. Chen, P.B. Armentrout, J. Phys. Chem. 100 (1996) 111.
[16] Y.-M. Chen, M.R. Sievers, P.B. Armentrout, Int. J. Mass Spectrom. Ion Processes 167/168 (1997) 195.
[17] M.R. Sievers, Y.-M. Chen, C.L. Haynes, P.B. Armentrout, Int. J. Mass Spectrom. Ion Processes 195/196 (2000) 149.
[18] L.S. Sunderlin, P.B. Armentrout, J. Am. Chem. Soc. 111 (1989) 3845.
[19] X.-G. Zhang, R. Liyanage, P.B. Armentrout, J. Am. Chem. Soc. 123 (2001) 5563.
[20] M.M. Armentrout, F.-X. Li, P.B. Armentrout, J. Phys. Chem. A 108 (2004) 9660.
[21] P.B. Armentrout, S. Shin, R. Liyanage, J. Phys. Chem. A 110 (2006) 1242.
[22] K.K. Irikura, W.A. Goddard III, J. Am. Chem. Soc. 116 (1994) 8733.
[23] M.C. Holthausen, C. Heinemann, H.H. Cornehl, W. Koch, H. Schwarz, J. Chem. Phys. 102 (1995) 4931.
[24] K.K. Irikura, J.L. Beauchamp, J. Am. Chem. Soc. 113 (1991) 2769.
[25] J.K. Perry, G. Ohanessian, W.A. Goddard, Organometallics 13 (1994) 1870.
[26] D.G. Musaev, K. Morokuma, Isr. J. Chem. 33 (1993) 307.
[27] S.K. Loh, D.A. Hales, L. Lian, P.B. Armentrout, J. Chem. Phys. 90 (1989) 5466.
[28] R.H. Schultz, P.B. Armentrout, Int. J. Mass Spectrom. Ion Processes 107 (1991) 29.
[29] E. Teloy, D. Gerlich, Chem. Phys. 4 (1974) 417.
[30] D. Gerlich, Adv. Chem. Phys. 82 (1992) 1.
[31] K.M. Ervin, P.B. Armentrout, J. Chem. Phys. 83 (1985) 166.
[32] P.J. Chantry, J. Chem. Phys. 55 (1971) 2746.
[33] C. Lifshitz, R.L.C. Wu, T.O. Tiernan, D.T. Terwilliger, J. Chem. Phys. 68 (1978) 247.
[34] B.L. Kickel, P.B. Armentrout, J. Am. Chem. Soc. 117 (1995) 4057.
[35] D.E. Clemmer, Y.-M. Chen, F.A. Khan, P.B. Armentrout, J. Phys. Chem. 98 (1994) 6522.
[36] C.L. Haynes, P.B. Armentrout, Organometallics 13 (1994) 3480.
[37] B.L. Kickel, P.B. Armentrout, J. Am. Chem. Soc. 117 (1995) 764.
[38] Y.-M. Chen, J.L. Elkind, P.B. Armentrout, J. Phys. Chem. 99 (1995) 10438.
[39] M.R. Sievers, Y.-M. Chen, P.B. Armentrout, J. Phys. Chem. 100 (1996) 54.
[40] T.A.M. Van Kleef, B.C. Metsch, Physica B & C. 95 (1978) 251.
[41] W.J. Chesnavich, M.T. Bowers, J. Phys. Chem. 83 (1979) 900.
[42] N. Aristov, P.B. Armentrout, J. Am. Chem. Soc. 108 (1986) 1806.
[43] P.B. Armentrout, in: N.G. Adams, L.M. Babcock (Eds.), Advances in Gas-Phase Ion Chemistry, vol. 1, JAI, Greenwich, 1992, p. 83.
[44] K.P. Huber, G. Herzberg, Molecular Spectra and Molecular Structure, vol. IV, Van Nostrand Reinhold, New York, 1979.
[45] T. Shimanouchi, Tables of Molecular Vibrational Frequencies; NSRDS-NBS39, Washington, DC, Consolidated Vol. I, 1972, p. 1.
[46] A.D. Becke, J. Chem. Phys. 98 (1993) 5648.
[47] C. Lee, W. Yang, R.G. Parr, Phys. Rev. B. 37 (1988) 785.
[48] M.J. Frisch, G.W. Trucks, H.B. Schlegel, G.E. Scuseria, M.A. Robb, J.R. Cheeseman, V.G. Zakrzewski, J.A. Montgomery Jr., R.E. Stratmann,

J.C. Burant, S. Dapprich, J.M. Millam, A.D. Daniels, K.N. Kudin, M.C. Strain, O. Farkas, J. Tomasi, V. Barone, M. Cossi, R. Cammi, B. Mennucci, C. Pomelli, C. Adamo, S. Clifford, J. Ochterski, G.A. Petersson, P.Y. Ayala, Q. Cui, K. Morokuma, P. Salvador, J.J. Dannenberg, D.K. Malick, A.D. Rabuck, K. Raghavachari, J.B. Foresman, J. Cioslowski, J.V. Ortiz, A.G. Baboul, B.B. Stefanov, G. Liu, A. Liashenko, P. Piskorz, I. Komaromi, R. Gomperts, R.L. Martin, D.J. Fox, T. Keith, M.A. Al-Laham, C.Y. Peng, A. Nanayakkara, M. Challacombe, P.M.W. Gill, B. Johnson, W. Chen, M.W. Wong, J.L. Andres, C. Gonzalez, M. Head-Gordon, E.S. Replogle, J.A. Pople, GAUSSIAN 98, Revision A.11, Gaussian, Inc., Pittsburgh, PA, 1998.

[49] M.J. Frisch, G.W. Trucks, H.B. Schlegel, G.E. Scuseria, M.A. Robb, J.R. Cheeseman, J.A. Montgomery, T. Vreven, K.N. Kudin, J.C. Burant, J.M. Millam, S.S. Iyengar, J. Tomasi, V. Barone, B. Mennucci, M. Cossi, G. Scalmani, N. Rega, G.A. Petersson, H. Nakatsuji, M. Hada, M. Ehara, K. Toyota, R. Fukuda, J. Hasegawa, M. Ishida, T. Nakajima, Y. Honda, O. Kitao, H. Nakai, M. Klene, X. Li, J.E. Knox, H.P. Hratchian, J.B. Cross, C. Adamo, J. Jaramillo, R. Gomperts, R.E. Stratmann, O. Yazyev, A.J. Austin, R. Cammi, C. Pomelli, J.W. Ochterski, P.Y. Ayala, K. Morokuma, G.A. Voth, P. Salvador, J.J. Dannenberg, V.G. Zakrzewski, S. Dapprich, A.D. Daniels, M.C. Strain, O. Farkas, D.K. Malick, A.D. Rabuck, K. Raghavachari, J.B. Foresman, J.V. Ortiz, Q. Cui, A.G. Baboul, S. Clifford, J. Cioslowski, B.B. Stefanov, G. Liu, A. Liashenko, P. Piskorz, I. Komaromi, R.L. Martin, D.J. Fox, T. Keith, M.A. Al-Laham, C.Y. Peng, A. Nanayakkara, M. Challacombe, P.M.W. Gill, B. Johnson, W. Chen, M.W. Wong, C. Gonzalez, J.A. Pople, Gaussian 03, Revision B.02, Revision B.02, Gaussian, Inc, Pittsburgh, PA, 2003.

[50] P.J. Hay, W.R. Wadt, J. Chem. Phys. 82 (1985) 299.

[51] G. Ohanessian, M.J. Brusich, W.A. Goddard III, J. Am. Chem. Soc. 112 (1990) 7179.

[52] M.C. Holthausen, M. Mohr, W. Koch, Chem. Phys. Lett. 240 (1995) 245.

[53] D. Andrae, U. Haeussermann, M. Dolg, H. Stoll, H. Preuss, Theor. Chim. Acta 77 (1990) 123.

[54] A. Simon, J. Lemaire, P. Boissel, P. Maitre, J. Chem. Phys. 115 (2001) 2510.

[55] K. Balasubramanian, D. Dai, J. Chem. Phys. 93 (1990) 7243.

[56] G. Gioumousis, D.P. Stevenson, J. Chem. Phys. 29 (1958) 294.

[57] F.-X. Li, X.-G. Zhang, P.B. Armentrout, J. Phys. Chem. B 17 (2005) 8350.

[58] J.K. Perry, Ph.D. Dissertation, California Institute of Technology, 1994.

[59] D.G. Dai, A.P. Huang, K. Balasubramanian, J. Mol. Spec. 154 (1992) 345.

[60] J. Simons, J. Nichols, Quantum Mechanics in Chemistry, Oxford University Press, New York, NY, 1997, p. 219.

[61] M.R. Sievers, Y.-M. Chen, P.B. Armentrout, J. Chem. Phys. 105 (1996) 6322.

[62] D.G. Musaev, K. Morokuma, J. Chem. Phys. 99 (1993) 7859.

[63] C. Peng, H.B. Schlegel, Isr. J. Chem. 33 (1994) 449.

[64] C. Peng, P.Y. Ayala, H.B. Schlegel, M.J. Frisch, J. Comp. Chem. 17 (1996) 49.

[65] C. Heinemann, R. Wesendrup, H. Schwarz, Chem. Phys. Lett. 239 (1995) 75.

[66] M. Pavlov, M.R.A. Blomberg, P.E.M. Siegbahn, R. Wesendrup, C. Heinemann, H. Schwarz, J. Phys. Chem. A 101 (1997) 1567.

[67] U. Achatz, M. Beyer, S. Joos, B.S. Fox, G. Niedner-Schatteburg, V.E. Bondybey, J. Phys. Chem. A 103 (1999) 8200.

[68] Y.-M. Chen, P.B. Armentrout, J. Am. Chem. Soc. 117 (1995) 9291.

[69] P.B. Armentrout, Y.-M. Chen, J. Am. Soc. Mass Spectrom. 10 (1999) 821.

[70] J.L. Elkind, P.B. Armentrout, Inorg. Chem. 25 (1986) 1078.